SYNTHESIS AND PROCESSING OF NANOSTRUCTURED BN AND BN/Ti COMPOSITES

by

ROBERT STEVEN HORVATH

A Dissertation submitted to the

Graduate School-New Brunswick

Rutgers, The State University of New Jersey

in partial fulfillment of the requirements

for the degree of

Doctor of Philosophy

Graduate Program in Material Science and Engineering

written under the direction of

Dr. Bernard H. Kear

and approved by

_____

_____

_____

_____

New Brunswick, New Jersey

JANUARY 2015

ABSTRACT OF THE DISSERTATION

Synthesis and Processing of Nanostructured BN and BN/Ti Composites

By ROBERT STEVEN HORVATH

Dissertation Director:

Dr. Bernard H. Kear

Superhard materials, such as cubic-BN, are widely used in machine tools, grinding wheels, and abrasives. Low density combined with high hardness makes c-BN and its composites attractive candidate materials for personnel and vehicular armor. However, improvements in toughness, and ballistic-impact performance, are needed to meet anticipated performance requirements. To achieve such improvements, we have targeted for development nanostructured c-BN, and its composites with Ti. Current research utilizes an experimental high pressure/high temperature (HPHT) method to produce these materials on a laboratory scale. Results from this work should transfer well into the industrial arena, utilizing high-tonnage presses used in the production of synthetic diamond and c-BN.

Progress has been made in: (1) HPHT synthesis of cBN powder using Mg as catalyst; (2) HPHT consolidation of cBN powder to produce nanostructured cBN; (3) reactive-HPHT consolidation of *mixed cBN/Ti* powder to produce nanostructured Ti- or TiB_2/TiN-bonded cBN; and (4) reactive-HPHT consolidation of *mixed hBN/Ti* powder to produce nanostructured Ti-bonded TiB_2/TiN or TiB_2/TiN. Even so, much remains to be done to lay a firm scientific foundation to enable the reproducible fabrication of large-area panels for armor applications. To this end, Rutgers has formed a partnership with a major producer of hard and superhard materials.

The ability to produce hard and superhard nanostructured composites by reacting cBN or hBN with Ti under high pressure also enables multi-layered structures to be developed. Such structures may be designed to satisfy impedance-mismatch requirements for high performance armor, and possibly provide a multi-hit capability. A demonstration has been made of reactive-HPHT processing of multi-layered composites, consisting of alternating layers of superhard Ti-bonded cBN and tough Ti. It is noteworthy that the pressure requirements for processing Ti-bonded cBN, Ti-bonded TiB_2/TiN, and their corresponding multi-layered structures are in the 0.1-1.0 GPa range, well within the capabilities of today's hot-pressing technologies; thus scaling this new reactive-HPHT processing technology seems assured.

Future research will focus on establishing mechanisms and kinetics of the various phase transformations observed during reactive-HPHT processing, with the objective of being able to optimize processing parameters to generate nanostructured cBN-based and TiB_2/TiN-based composites that display superior mechanical properties, particularly under high-strain-rate conditions.

Dedication

I would like to dedicate this thesis to the memory of three people very close to my heart.

My late Mother Dianne Horvath whose 30+year career in education inspired me to be something more than a professional, to devote my life to an occupation that has rewards above and beyond monetary compensation. We miss you every day.

My Brother from another mother, the late Dr. Howard Fritz. Howie had been there, so he knew how to talk about it, and then suddenly he was gone. God Bless you Howie.

My close personal friend the late Laura Giaquinto Ballesteros, whose heroic yet tragic battle with cancer is an inspiration to us all. We love you Laura.

Acknowledgements

This research endeavor was made possible through the guidance, direction, and funding provided by Dr. Bernard H. Kear, and Dr. Stephen D. Tse, graduate research advisers. Significant contributions were also made by Dr. Oleg Voronov of Diamond Materials Inc. with respect to sample preparation, processing and considerable technical insight. Also, I would like to extend my gratitude to Dr. Thomas Tsakalakos for contributions to this venture through his technical insight. Also, I would like to thank Dr. Jafar Al-Sharib for TEM and technical contributions. The guidance and support provided by Dr. Richard Lehman, Dr. Lisa Klein, and Dr. Rich Haber toward my graduate school and professional ventures and their ability to find creative solutions to my unique situation has been greatly appreciated.

I would like to acknowledge my family for their support patience, and encouragement;

Andrew Horvath Charles M. Horvath
Christian Horvath Anne M. Horvath
Juliana Horvath Charles J. Horvath
Angelina Horvath

Most of all , I would like to thank my companion Ms. Janet Scherer, for her unwavering love, support and motivation. Words can not express my gratitude, Thank you all.

Table of Contents

List of Tables

List of Figures

A. Overview

Cubic-boron nitride (cBN) is widely used in machine tools, drill bits, and grinding wheels [1-4]. Recently, interest has developed in its potential for lightweight personnel and vehicular armor. Currently, the preferred materials are B_4C and SiC. Because of its much higher hardness and stiffness, cBN is an attractive alternative for next generation armor. However, to ensure superior ballistics performance, its fracture toughness needs to be improved, without seriously compromising hardness and strength.

To realize such properties, we have been investigating high pressure/high temperature (HPHT) methods to produce: (1) nanostructured cBN, since it is known that hardness and toughness increase with decreasing grain size; and (2) nanostructured Ti-bonded cBN, where the presence of the metal-binder phase imparts toughness, as in Co-bonded WC. Progress has been made in both areas, but the discovery of a new processing route to produce BN/Ti-base nanocomposites under reduced-pressure conditions is perhaps most significant, since it enables HPHT powder-processing technology to be scaled. Thus, there is the prospect of being able to fabricate large-area superhard armor panels in a cost-effective manner. However, much remains to be done to optimize processing parameters to make this a commercially-viable technology. Presently, a 300-ton force press, located at Diamond Materials Inc. (DMI), is used to make small disc-shaped pieces (typically 4-mm dia. x 3 mm) for characterization and testing purposes. Looking ahead, the goal is to fabricate a 1-meter square demonstration armor panel, which will be achieved using a 10,000-ton force press at Diamond Innovations - a leading company in the hard and superhard materials industry.

As will be shown, under varying HPHT processing conditions, Ti can either bond directly to cBN to form a superhard Ti-bonded cBN composite or react with cBN to form a superhard TiB_2/TiN-bonded cBN composite. In the latter case, it is significant that the reaction occurs at reduced pressures, thus enabling scaling of the technology. Similar pressure-controlled reactions occur between hBN and Ti. In particular, a fully dense hard Ti-bonded TiB_2/TiN composite is produced via control of an *exothermic reaction* that accompanies the powder-consolidation process, here described as *reactive-HPHT* (r-HPHT) consolidation. A significant advantage of using hBN powder as starting material is its low cost relative to cBN powder. Similar reactions are anticipated between mixed BN and Al and/or Mg powders under r-HPHT processing conditions.

The ability to produce hard and superhard composites by reacting cBN or hBN with Ti under high pressure also enables multi-layered structures to be developed. In principle, such structures may be designed to satisfy impedance-mismatch requirements for high performance armor, and possibly provide a multi-hit capability. A demonstration has been made of r-HPHT processing of a multi-layered composite that consists of alternating layers of superhard Ti-bonded cBN and tough Ti. Compositional grading of the interphase interfaces occurs quite naturally during processing, which ensures good bonding between the dissimilar materials[5]. It is noteworthy that the pressure requirements for processing Ti-bonded cBN, Ti-bonded TiB_2/TiN, and their corresponding multi-layered structures, are as low as 0.1-0.3 GPa, which are well within the capabilities of today's hot-pressing technologies; thus scaling this new r-HPHT technology seems assured.

In this research project, progress has been made in: (1) HPHT synthesis of cBN powder using Mg as catalyst; (2) HPHT consolidation of cBN powder to form nanostructured cBN;

(3) r-HPHT consolidation of mixed cBN/Ti powder to produce nanostructured Ti- or TiB_2/TiN-bonded cBN composites; (4) r-HPHT consolidation of mixed hBN/Ti powder to produce nanostructured Ti-bonded TiB_2/TiN or TiB_2/TiN composites; and (5) r-HPHT fabrication of a demonstration multi-layered structure, comprising alternating layers of superhard Ti-bonded cBN, hard TiB_2/TiN, and tough Ti. As noted above, such a layered composite offers considerable flexibility in the design of armor to satisfy specific ballistics requirements.

Table 1 presents published data on the grain-size dependence of hardness and toughness of cBN. It is noteworthy that reducing the grain size of cBN from micro- to nano-scale dimensions increases both hardness and toughness. The increase in hardness is ascribed to the well known Hall-Petch effect[6], whereas the increase in toughness is ascribed to the difficulty of propagating a crack through a nano-grained material. In general, the crack follows a tortuous path along the weaker grain boundaries rather than through the nano-grains themselves via cleavage fracture. A similar mechanism explains the high hardness and toughness of nano-twinned cBN.

Table 1 - Properties of selected hard and superhard materials [7-16]

Description	Hardness (GPa)	Modulus (GPa)	Toughness ($MPa.m^{1/2}$)
Micro-grained cBN	33-45	909	6.8
Nano-grained cBN	85	-	10.5
Nano-twinned cBN	108	-	12.7
TiN	18-24	350-450	4.3
TiB_2	25-35	350-550	3.3

Even though nanocrystalline c-BN displays higher hardness and toughness than its microcrystalline counterpart, it seems unlikely that the toughness will be sufficient to avoid

c*oarse-scale fracturing* during ballistic impact, accompanied by little energy absorption. On the other hand, a Ti-bonded c-BN composite, comprising a high fraction of superhard c-BN particles uniformly dispersed in a much tougher Ti binder phase should experience *fine-scale fracturing*, and therefore greater energy absorption. For example, a 70:30 c-BN:Ti composite should exhibit superior hardness and modest toughness, whereas a 30:70 c-BN:Ti composite should exhibit modest hardness and superior toughness. Moreover, a multi-layered structure, comprising alternating superhard, hard, and ductile layers should provide even greater energy absorption, and further enhance ballistics performance. However, much remains to be done to optimize processing parameters to realize superior performance for multi-layered composites with compositionally-graded interface~~s~~. Looking ahead, it is anticipated that the mechanical performance of a multi-layered structure, comprising alternating layers of superhard Ti-bonded cBN, hard Ti-bonded TiB_2/TiN, and tough Ti (or its alloys), can be designed to meet the performance requirements of most personnel and vehicular armor applications[17].

These considerations provided the primary motivation for the present research on synthesis and processing of nanostructured BN and BN/Ti composites for lightweight armor. As will be shown, a successful demonstration of HPHT consolidation of cBN powder to form nanocrystalline-cBN has been made, but only at very high pressures, 5.0-8.0 GPa. Such processing conditions are accessible using today's industrial-scale HPHT presses [18], but scaling to 5-cm diameter is about the practical size limit [19]. To overcome this scaling limitation, on-going research is investigating methods to reduce the pressure requirements into the scalable range, preferably <2.0 GPa. A promising approach

is to use plasma-synthesized nanopowder as a sintering aid to consolidate powder compacts of micron-size cBN powder.

Concurrently, research continues on r-HPHT processing of Ti-bonded cBN and Ti-bonded TiB_2/TiN composites, inspired by the discovery made herein that nanostructured hard and superhard BN/Ti composites can be produced at pressures as low as 0.1-0.3 GPa, which places no practical limits on scaling the process using today's hot-pressing equipment. Moreover, the introduction of controlled distributions and volume fractions of Ti as binder phase should provide needed fracture toughness. In the case of a multi-layered structure, comprising alternating layers of superhard Ti-bonded cBN, hard Ti-bonded TiB_2/TiN, and tough Ti, another singular benefit is the flexibility afforded in armor design and fabrication. For example, only the outer layer facing an incoming projectile needs to be made of superhard Ti-bonded cBN; underlying or backing layers may be made of less costly hard/tough Ti-bonded TiB_2/TiN and tough Ti or its alloys. So far, a first demonstration has been made of the ability to fabricate such a layered composite, with the ability to control structure at nano-scale dimensions. Much remains to be done to produce an end-product, say in the form of a large-area armor panel that satisfies the stringent requirements with respect to ballistics performance, but it now seems achievable.

Superhard machine tools, in various sizes and shapes are widely employed in manufacturing. An important market niche is held by cBN, since it is much better than diamond in resisting degradation in high-speed machining, where the tool/workpiece interface gets very hot. If this problem is severe enough, as in machining of many hardened steels and nickel-base superalloys, then cBN tools are preferred, since diamond tools rapidly wear out by reaction with the workpiece itself and/or by oxidation [12]**.** Hence,

another important outcome of this research is a new class of nanostructured superhard/tough cBN tools that resist degradation at high machining speeds, even when the tool/workpiece interface gets white hot! An immediate impact in high-speed machining of nickel-base superalloys is expected, since there the need is greatest and potential pay-off significant.

B. Relevant Prior Research

Pioneering research, conducted by H.T. Hall[3], has shown that the transformation of hBN to cBN occurs at 5.0-9.0 GPa/1500-2000°C in the presence of Mg, apparently acting as a catalyst or activator. The fully consolidated cBN has high hardness, easily scratches B_4C, and is insoluble in most acids. Wentorf [4] also reported that Li and Al are also effective catalysts, but, unlike diamond, Fe, Ni and Mn are not. In the absence of a catalyst, Bundy and Wentorf [2] found that the conversion of hBN to cBN occurs at a minimum pressure of 11.5 GPa at 1730°C.

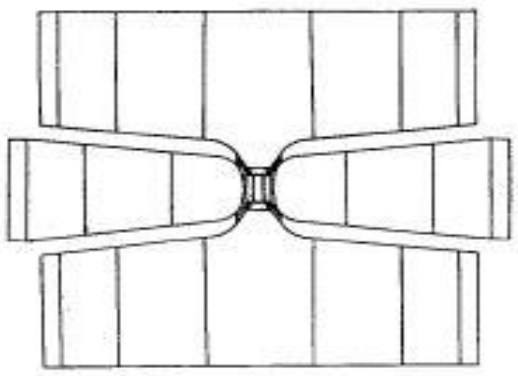

Figure 1 - Schematic of early HPHT apparatus used by H.T. Hall[3]

When processing is conducted at the highest temperature and pressure close to the hexagonal-to-cubic phase equilibrium line crystallite size is large, apparently due to the increased thermodynamic driving force, but crystallite quality is poor. Surfaces of large tetrahedral- and octahedral-shaped cBN crystallites formed at high rates show growth steps and ledges, and at the highest rates twinning is observed [3]. The color of the cBN particles, which varies from white to black, is attributed to differences in the material's stoichiometry. Since the discovery of cBN, various superhard materials have been developed to fill the gap in hardness between cBN and diamond. For example, metastable

forms of superhard BC_2N and has been reported [20], as well as B_6O and $B_{13}N_2$ phases. All these compounds have structures similar to diamond and cBN.

Hibbs and Wentorf [2] were first to develop applications for *monolithic or bulk* diamond and cBN. For machine tools and drill bits requiring good fracture toughness, thin layers of superhard materials are bonded to supporting strong/stiff WC/Co substrates. Processing parameters are 5.0-7.0 GPa at 1500-2000ºC, and grain sizes are 2.0-100 µm. ***Table 2*** shows, for several applications, superior machining performance of such Compax tools relative to conventional WC/Co cemented-carbide tools.

Table 2 - Cutting tool performance of diamond and cBN relative to WC/Co cemented carbide [2]

Material	Total number of pieces cut per tool
Machining silicon-aluminum SAE 332	
Compax diamond tool	412,000
Cemented carbide	2,400
Turning rubber filled with nickel and aluminum powder	
Compax tool	6,000
Cemented carbide	140
Machining flame-sprayed alloys (Colmonoy No. 43)	
CBN tool	3,000
Cemented carbide	9
Milling of type 380 aluminum line bore crankcase	
Compax tool	12,000 to 14,000
Cemented carbide	3,000
Machining glass filled polypropylene (facing operation*)	
Compax tool	7,000
Cemented carbide	400

*Cutting speed for Compax is approximately two times that of carbide.

In a recent publication [12], Solozhenko et al. report the successful processing of *bulk nanocrystalline cBN* (grain size 10-30 nm) via the direct (non-catalytic) transformation of hBN at 20 GPa/1500ºC. Vickers hardness of the resulting cBN is 85 GPa, inset in ***Figure 2***, and its grain size is 10-30 nm. When the processing temperature is raised to increase the grain size to 300-400 nm, the hardness is reduced to 50 GPa, ***Figure 2***, this value is typical of today's commercial micro-grained cBN. This trend is in accord with the Hall-Petch relationship, indicating that plastic deformation (slip and/or twinning) is severely restricted in an ultra-fine nanocrystalline structure[21]. The fracture toughness of nano-cBN is K_{1C} = 10.5 MPa $m^{1/2}$, higher than values, K_{1C} = 2.8-6.8 MPa $m^{1/2}$, for all known superhard BCN-type phases. Thus, nano-cBN is harder and tougher than micro-cBN, and all related superhard phases [12]**.**

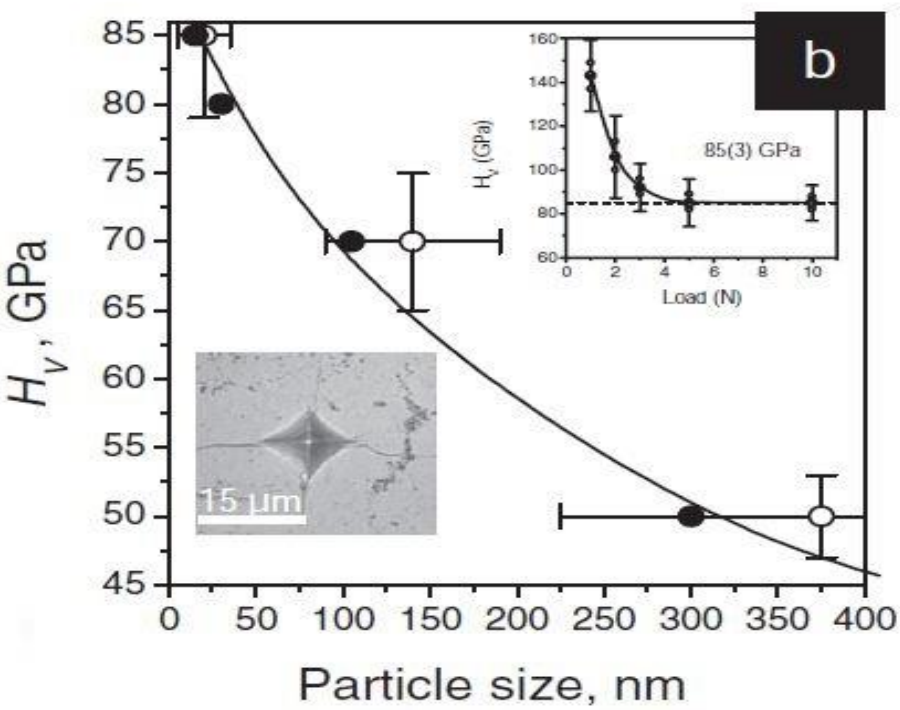

Figure 2 - Effect of nanoscale grain size on Vickers hardness of cBN[12]

Nano-cBN also displays thermal and chemical stability superior to diamond. For example, thermo-gravimetric analysis shows that nano-cBN is more resistant to oxidation than nano-diamond, ***Figure 3***. The onset temperature for oxidation is 1460ºK for nano- and micro-cBN, which compares with 950ºK for nano-diamond. This difference in behavior is due to the formation of a relatively stable surface-passivation film of B_2O_3 on cBN, whereas diamond reacts with ambient air to form CO_2; in other words the diamond surface experiences gasification. Under high vacuum conditions or in an inert atmosphere diamond is stable up to about 1500ºK., then phase decomposition yields graphitic material.

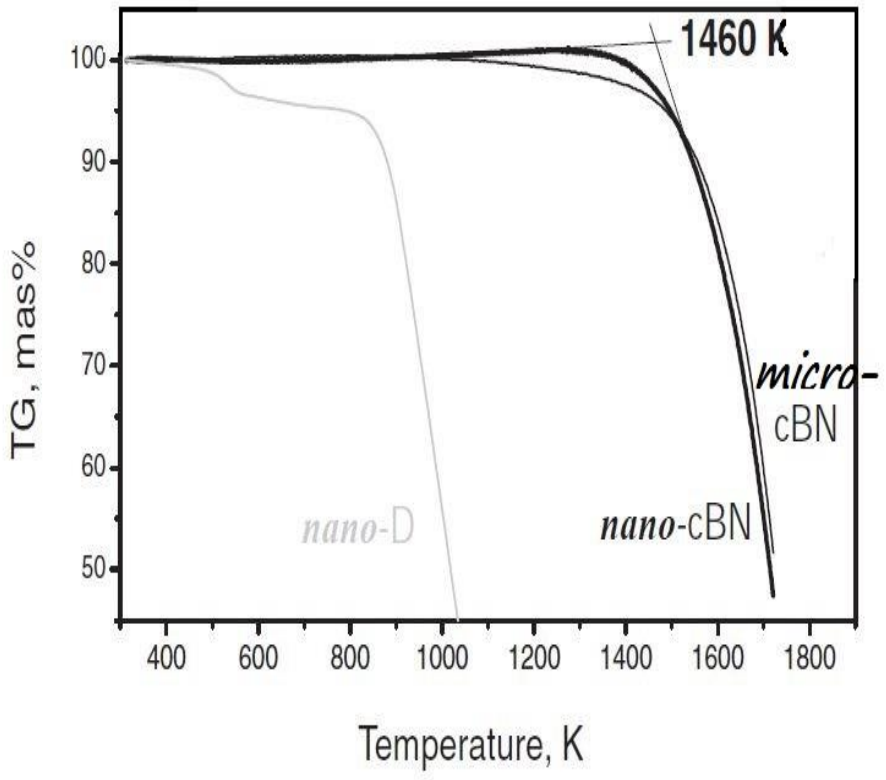

Figure 3 - Thermal stability of nano-cBN relative to nano-diamond[12]

C. Crystal Structures and Properties

C.1 Boron nitride

At ambient pressure hBN is the stable phase, but at higher pressures and temperatures hexagonal BN transforms to cBN**,** ***Figure 4***. The latter, once formed, can be retained at ambient pressure in a metastable state. However, to retain cBN after HPHT processing, fast cooling and reduction in pressure is necessary; otherwise it reverts back to hBN. In practice, an activator or catalyst is used to promote the transformation of hBN into cBN. Subsequent experimental and theoretical work led to the now generally accepted phase diagram shown in ***Figure 5***[23]**.**

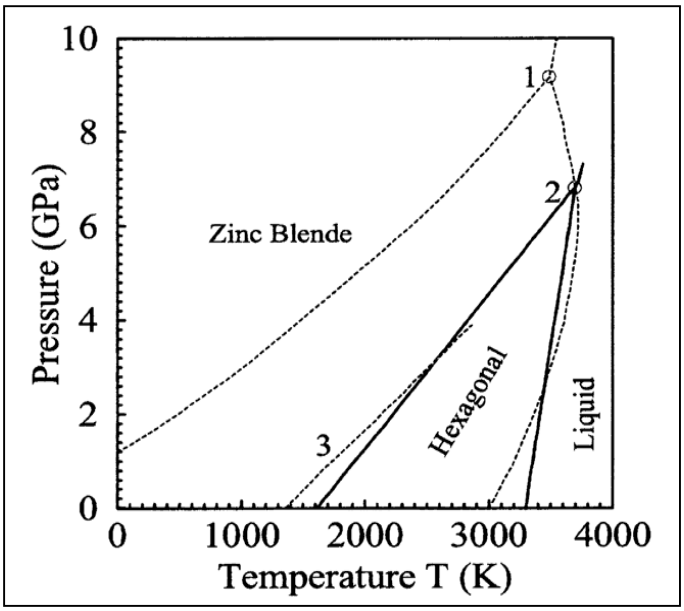

Figure 4 - Bundy-Wentorf's phase diagram for BN [23]

***1, Bundy-Wentorf's diagram; 2, Equilibrium diagram; 3, h*-BN <=> c-BN boundary line (Solozhenko, 1994).**

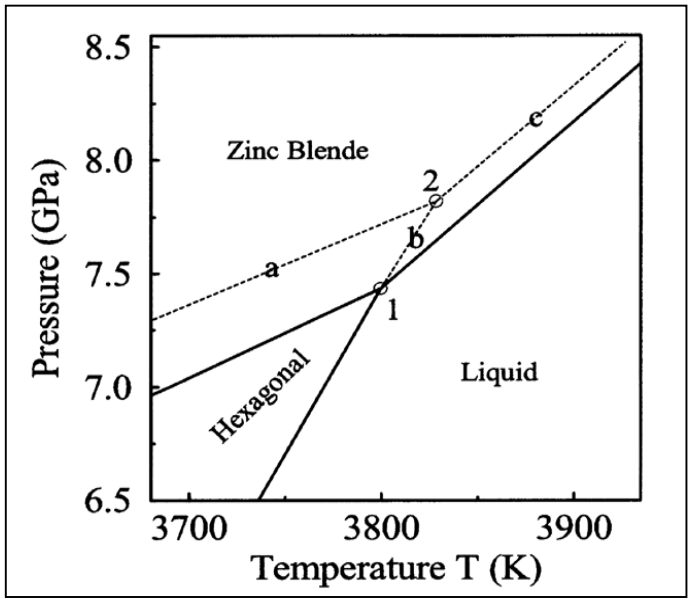

Figure 5 - Equilibrium phase diagram for BN[23]

1 is hexagonal-zinc blende (cubic)-liquid triple point; 2 metastable hexagonal-wurtzite-liquid triple point; a) line of wurtzite metastable equilibrium; b) line of metastable hexagonal melting; c) line of metastable wurtzite melting. (Solozhenko et al. 1998)

The *hexagonal* structure of BN (hBN), **Figure 6**, has a ring-like arrangement of covalently-bonded boron and nitrogen atoms within one atomic layer, with each such layer bonded to adjacent layers by weak Van der Waals bonds.

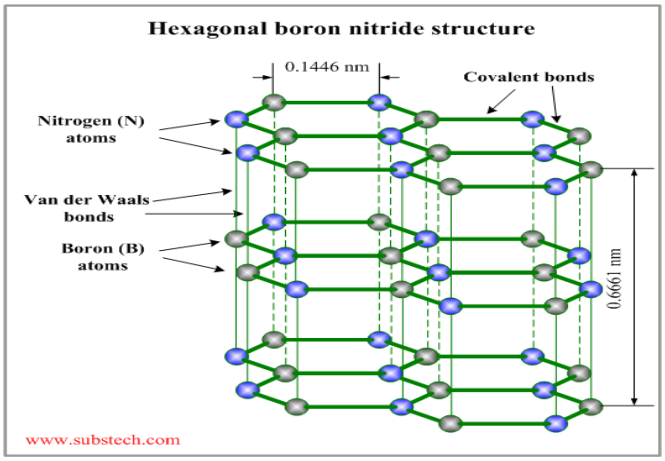

Figure 6 - Hexagonal structure of boron nitride [24]

The *wurtzite* structure of BN (wBN), ***Figure 7***, is an example of a hexagonal structure that is common to many binary compounds, including other hard phases, such as α-SiC, GaN, and AlN[25].

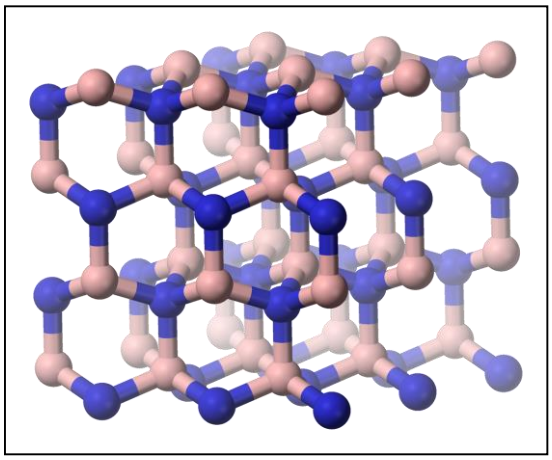

Figure 7 - Wurtzite structure of boron nitride[26]

The *cubic* structure of BN (cBN), ***Figure 8***, comprises two interpenetrating face-centered cubic lattices. Each atom in one lattice is covalently bonded to four nearest neighbor atoms of the opposite type in the other lattice. The cBN structure is common in binary compounds, and is often referred to as the zinc blende structure.

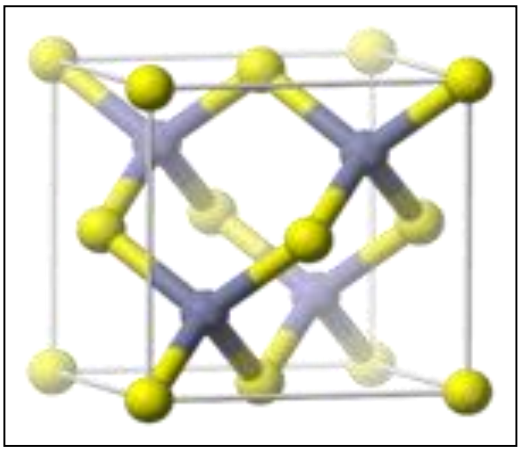

Figure 8 - Cubic structure of boron nitride [27]

C.2 Titanium diboride

The *hexagonal structure* of titanium diboride (TiB_2), ***Figure 9***, consists of planar stacking of strong *covalently-bonded* Ti and B atoms; as such, it has an exceptionally high melting point, 3215°C. It also has high hardness and stiffness, ***Table 1***, but applications are limited by the high temperature required for powder consolidation. If not properly controlled, anisotropy in thermal expansion misfit between a and c axis of the hexagonal structure can cause catastrophic failure during cool-down after sintering, at least for large-grained material. Fully dense fine-grained TiB_2, however, has been produced by hot pressing, hot isostatic pressing, microwave sintering, and dynamic compaction[28], but applications are still limited to a few commercial products: impact-resistant armor, heat-resistant crucibles, and wear-resistant coatings.

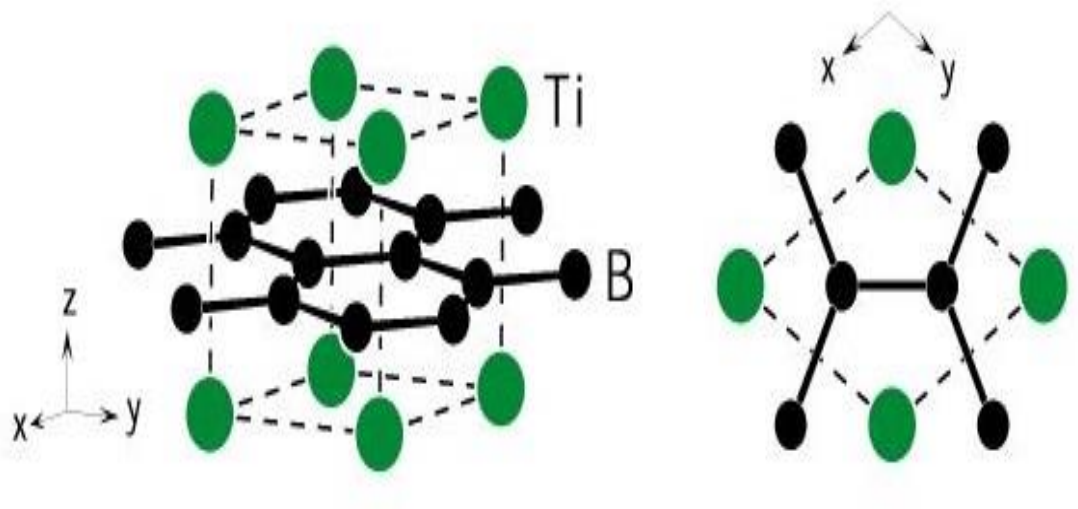

Figure 9 - Hexagonal crystal structure of TiB_2 [29].

Flexural strength of TiB_2 increases with decreasing grain size, ***Figure 10***, in accord with the Hall-Petch relationship, but there is no data available for sub-micron or nano-grained material. Data for elastic modulus, ***Figure 11***, illustrates its sensitivity to the relative density of the sintered product. For a high density, relatively pore-free product the modulus is ~550 GPa; upper limit shown in ***Table 1***.

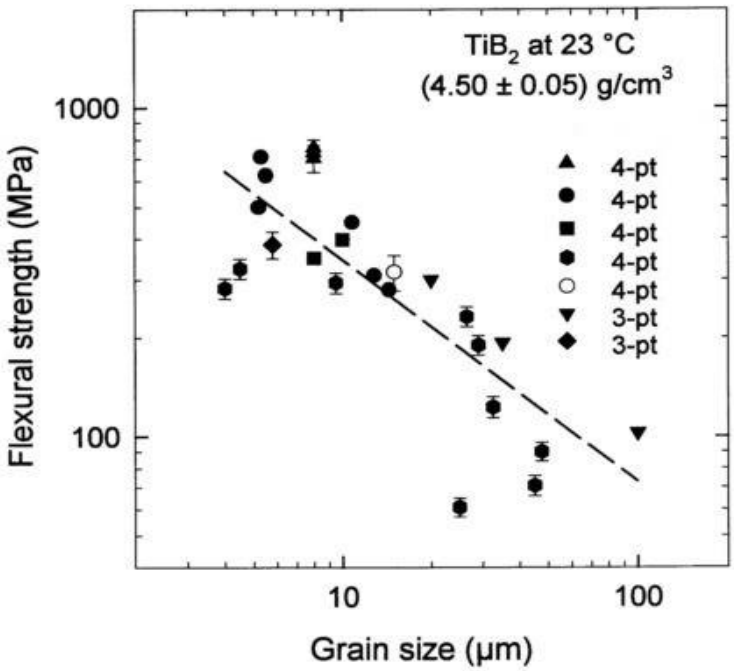

Figure 10 - Flexural strength of TiB_2 as a function of grain size [14]

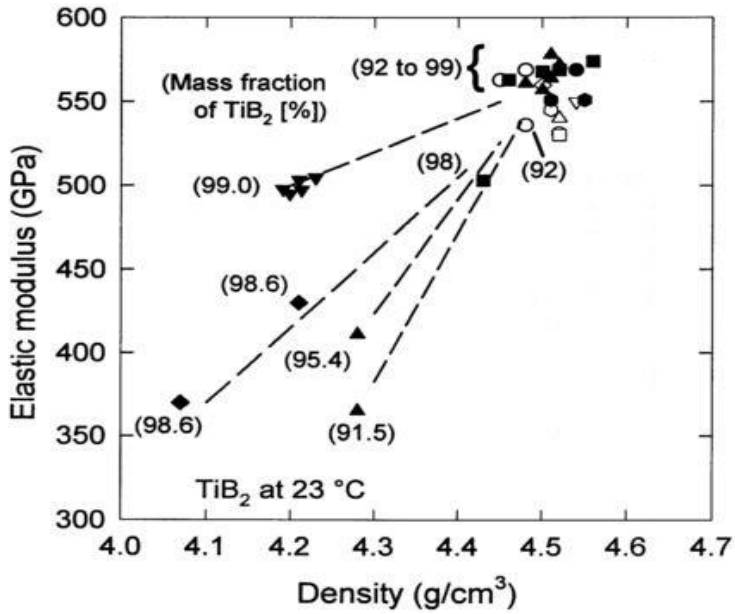

Figure 11 - Elastic modulus of TiB_2 as a function of density [14]

Reported values for fracture toughness of TiB_2, ***Figure 12***, indicate variability due to variations in grain size, measurement method, and chemical purity. Relatively small percentages of second phases are often present in sintered TiB_2, resulting from raw materials purity or intentionally added sintering aids to mitigate the effects of shrinkage anisotropy. Fracture toughness is optimal at 98% pure TiB_2, with density 4.5 g/cm^3 and grain size 5-10 µm, and has a value $K_{1C} = 6.2$ MPa·m$^{1/2}$. Interestingly, this toughness value, unlike that for elastic modulus and flexural strength, is not inversely proportional to grain size, but optimal at a median grain size value.

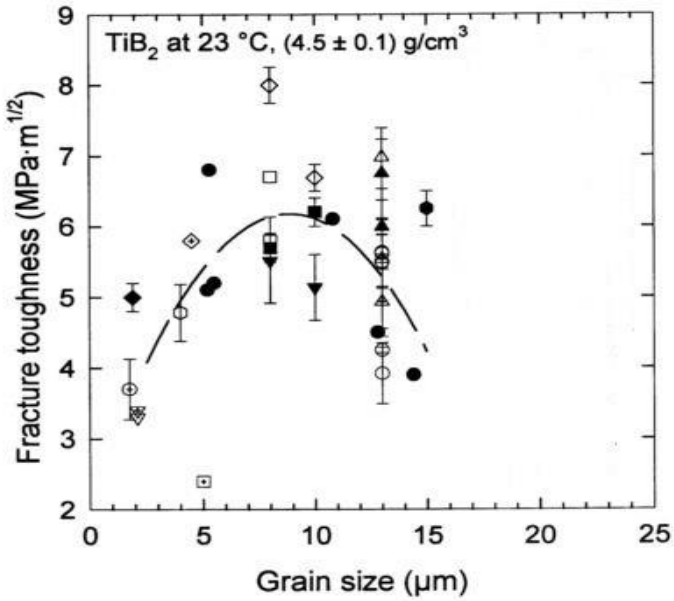

Figure 12 - Fracture toughness of TiB_2 as a function of grain size[14]

Measurements of Vickers hardness of TiB_2 do not show a strong dependence on grain size. However, there is a considerable level of variability in the reported data that is attributed to variations in the applied load, ***Figure 13***. In order to more completely define the true relationship between grain size and hardness for TiB_2, much more work needs to be done, which is beyond the scope of the present research.

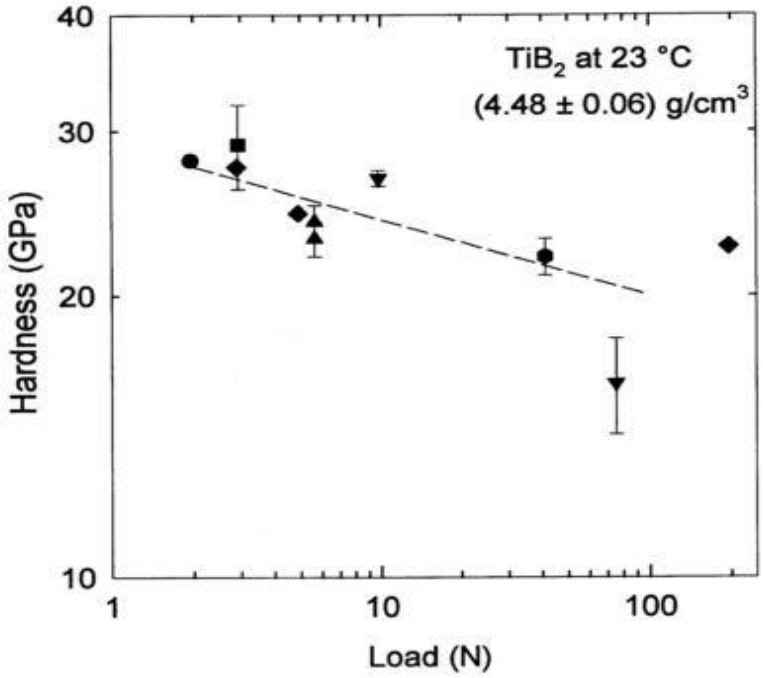

Figure 13 - Hardness of TiB_2 versus applied load[14]

C.3 Titanium nitride

The *cubic structure* of titanium nitride (TiN), with coordination identical to NaCl, is depicted in ***Figure 14***. It has a strong covalently-bonded structure, which is reflected in its exceptionally high melting point, 3290ºC. Its density, calculated from lattice parameters and assuming zero porosity, is 5.495 g/cm^3. At a relative density of 96% the reported value of elastic modulus is 450 GPa [7]. TiN also displays exceptional wear and corrosion resistance, and hence is widely used in industrial coatings, but there is little demand for bulk materials[30].

In a recent studies of bulk TiN [31], prepared by hot pressing at 1723-2023ºK for 60-1500 sec, reliable measurements of mechanical properties have been obtained. Vickers hardness, after polishing under an applied load of 0.98 N is Hv = 24 GPa, whereas fracture

toughness after processing at 2023°K/16.6 MPa is K_{1C} = 4.28 MPa ·$m^{1/2}$. Based on these experiments, it now seems possible to produce bulk TiN structures with reproducible and attractive properties.

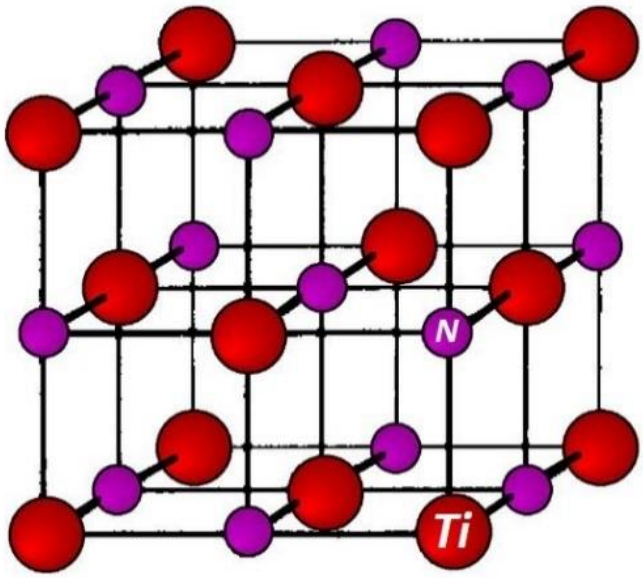

Figure 14 – Cubic crystal structure of (TiN)[32]

D. Experimental Methods

In what follows, a description is given of the high pressure/high temperature (HPHT) apparatus used throughout this research to synthesize nanostructured BN and BN/Ti composites. A detailed description of the HPHT apparatus is presented, as well as methods used for its calibration[33].

D.1 Apparatus

All HPHT experiments were performed at Diamond Materials Inc. (DMI) - a spinoff company from Rutgers' Center for Nanomaterials Research (Rutgers' CNR). DMI's apparatus provides a highly flexible experimental platform, allowing systematic studies of the influence of critical processing parameters - pressure, temperature and holding time - on the resulting structures, phases, and properties of the consolidated materials. Experience has demonstrated that this system yields reproducible results over a wide range of processing parameters, 1-10 GPa/20-2000ºC.

Figure 15 shows a schematic of DMI's HPHT apparatus, as described in considerable detail in U.S. Patent 8,021,639 B [34]. Briefly, it consists of a matching pair of WC/Co anvils and inserts, which are reinforced with pre-stressed steel rings. The arrangement enables pressures to be applied that are higher than the compressive strength of the anvil material. The reaction cell consists of a resistively-heated graphite crucible and insulating ceramic spacers. A critical component is the pressure-transmitting medium, which consists of deformable ceramic that is machined to match the profiles of the anvils. Under high pressure, the plastically deformed ceramic exerts a strong restraining force on the reaction

cell, thus generating a high pressure in its working volume [35]. This is used routinely to synthesize high pressure phases and to consolidate powders.

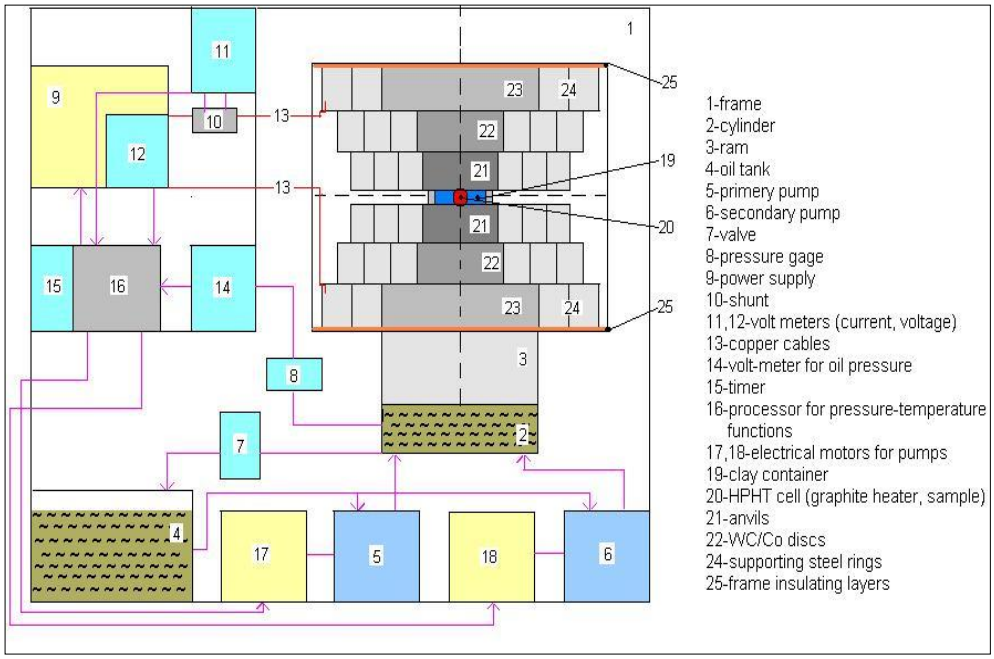

Figure 15 - Schematic of HPHT apparatus[36]

D.2 Calibration

Pressure is calibrated at ambient temperature for several known phase transitions in solid materials, ***Table 3***. Variation in the electrical resistivity as a function of pressure signals that a phase transition has taken place. The dependence between loading force and resistivity allow for precise calibrations to be made [35]. Temperature is calibrated via known values of melting temperatures of different substances under high pressure. Under ideal conditions, a sharp increase in electrical resistance of the reaction cell signals that melting has occurred. In practice, the voltage drop across the reaction cell gradually increases as melting occurs, and changes in current are measured [36][37].

Table 3 - Pressure dependence of phase transitions in several materials at ambient temperature.[36]

Material	Pressure (GPa)	Material	Pressure (GPa)
Ce	0.80 ±0.02	Yb	4.0 ±0.1
Bi I	2.55 ±0.01	Ba I	5.5 ±0.1
Bi II	2.69 ±0.01	PbSe (R	5.9 ±0.7
PbSe (R	3.60±0.50	Bi III	7.7 ±0.0
Ti	3.67 ±0.05	Sn	9.4 ±0.0

Figure 16 shows the pressure-force calibration curve for HPHT apparatus at room temperature. P* is the pressure in hydraulic cylinder of the press. F is the force corresponding to P*, generated by the press and applied to HP unit. P is the pressure in the reaction cell of the HP apparatus at a given force F. ***Figure 17*** depicts the temperature-electrical power curve for calibration of HPHT apparatus by melting several metals under high pressure. Power (W) of the electrical current is W (Watt) = U(Volts) x I(Amps). Values U and I are measured with high precision. Blue line is approximate values, red and pink lines indicate possible errors, as estimated by DMI.

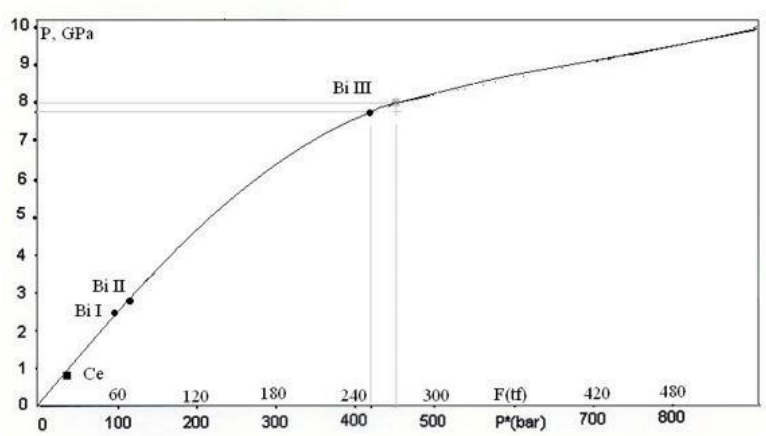

Figure 16 – Pressure-force calibration for HPHT apparatus [34]

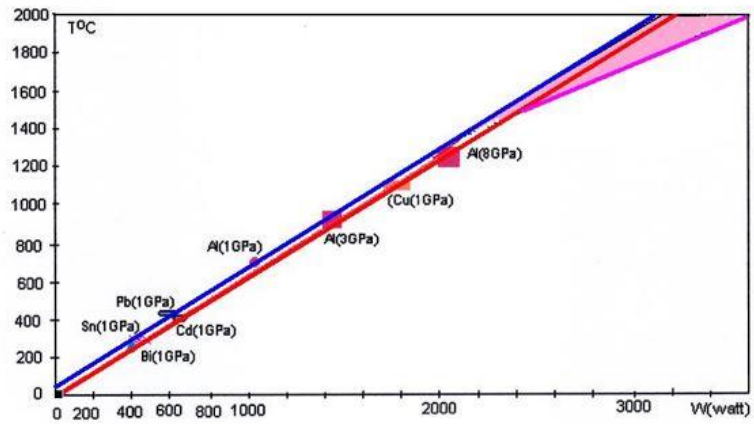

Figure 17 - Temperature-power curve for calibration of HPHT apparatus[38][36]

D.3 Procedure

A typical HPHT processing procedure is illustrated in ***Figure 18***. About 200 mg of the powder of interest, e.g. BN or BN/Ti blend, is placed in the reaction cell, pressure is increased to the desired level (I), temperature is increased at 70°C per minute (II), held for a prescribed dwell time (III), cooled under pressure at 70°C per minute (IV), and finally the pressure is released to ambient (V).

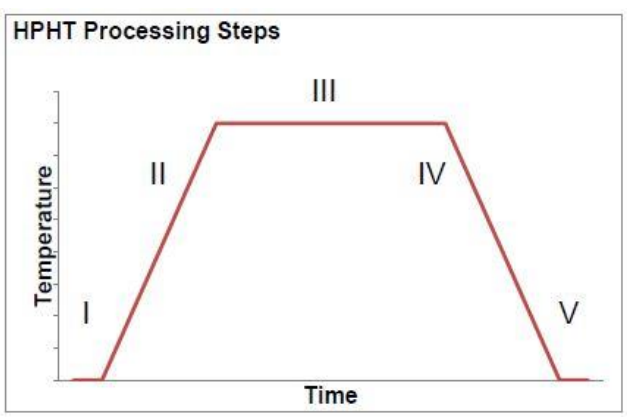

Figure 18 - Typical HPHT processing cycle

E. Characterization Techniques

E.1 X-ray diffraction

In order to analyze phase composition and estimate mean crystallite or domain size, often referred to as coherent scattering domain (CSD) size, which may be smaller or equal to the grain size, X-ray diffraction analysis is employed [39]. In this investigation, a Panalytical Xpert-Pro diffractometer system, with Cu-Kα radiation of wavelength $\lambda = 1.54059$Å and Pixcel type multi-channel detector is used for phase analysis and crystallite size determinations. Calculations are made with Jade Software Ver. 9.6.0 4-11-14 [40], using an Inorganic Crystal Structure Database (ICSD) released in 2014 [41].

After HPHT processing, samples are fractured and crushed using a hardened-steel chisel and plate. The finely crushed powder is placed on a Si substrate in a Zero Background Holder (ZBH). The sample holder is 32-mm diameter x 2-mm thick, with a 15-mm diameter x 0.2-mm deep depression for placement of the powder sample. A sample-analysis protocol is used to attain sufficient signal intensity and low background, i.e. a signal-to-noise ratio that permits quantitative analysis with Jade software package[42]. The sample is rotated in the incident beam to ensure diffraction from all the differently oriented particles in a powder compact, thereby ensuring multiple reflections for all crystallographic orientations with sufficient diffracted beam intensity. In this study, a wide 2θ-scan is used to capture a secondary diffraction peak for cBN located at 89.81^{o}, allowing positive phase identification. The Jade X-ray diffraction software uses the Scherrer equation to estimate the size of the coherent scattering domain (CSD), which is generally accepted to be a reasonable estimate of grain size of an inorganic solid.

The Scherrer equation can be written as [39]

$$t = \frac{0.94\lambda}{\beta \cos\theta}$$

where t is coherent scattering domain or crystallite size, λ is wavelength of the incident beam, θ is Bragg angle, and β is line broadening of the diffraction peak at full width half maximum (FWHM). The equation is limited in its applicability to 100-nm maximum grain size. To provide confirmation of measured grain size, direct observation by TEM and SEM is used.

Numerous factors contribute to the line-broadening of a diffraction peak and it is important that the calculated value of the coherent scattering domain (CSD) or crystallite size be recognized as a lower boundary only[43-44]. Since instrumental broadening is minimal for the system used, the most significant contributions to peak broadening are: (1) inhomogeneous strains in the material, and (2) the presence of crystal imperfections, such as dislocations, stacking faults, twins, grain boundaries, chemical heterogeneities, and a wide distribution of crystallite size. These contributions can also cause distortions of the peak shape. If all of the sample contributions are zero then the Scherrer equation applies. Conversely when these effects are non-zero the Scherrer equation is an indicator of the lower boundary of the coherent scattering domain [45].

Ghosh et al. [46] presents data on the effects of milling time on hexagonal-BN. In this work, Scherrer, Williamson-Hall, and Rietveld techniques are used to determine contributions to line broadening and shape from crystallite size, lattice strains, stacking faults, and dislocation density. All of these analytical techniques require the use of

specialized computer software and considerable expertise in application and interpretation. The authors conclude that at milling times <5 hours the major effects are actually due to grain size reduction. At greater than 17 hours of milling time the contributing factors are lattice strains, and at intermediate milling times it is a combination of grain size reduction and lattice strain. The results of their analysis are verified by analytical electron microscopy techniques.

To further validate the crystallite size (coherent scattering domain size) calculations based upon the Scherrer equation at FWHM for powder #1 and #2 following HPHT processing, Jade software is utilized to facilitate a generalized Williamson-Hall plot for determination of size and strain, whereby the magnitude of the crystallite size and micro-strain are obtained. The Williamson-Hall plot separates contributions from stress, strain, and lattice distortions from the crystallite size. This analytical technique relies on the fact that size broadening (β_L) varies as a function of $1/\cos\theta$, and strain broadening (β_e) as function of $\tan\theta$. When these contributing factors are quantified and plotted as a function of $\sin\theta$ vs. $\beta\cos\theta$, the y-intercept is the size value, and the slope is the strain component, **Figure 19**. This analysis allows crystallite size to be separated from peak broadening due to microstructural stress, strain, and others factors**.** Significant deviation of the data points from the projected line would indicate factors other than the crystallite size contributing to peak broadening and negate the analysis. This technique is applied successfully for a select group of samples and used to verify the crystallite size calculated from the Scherrer formula and is found to be reasonably consistent[47].

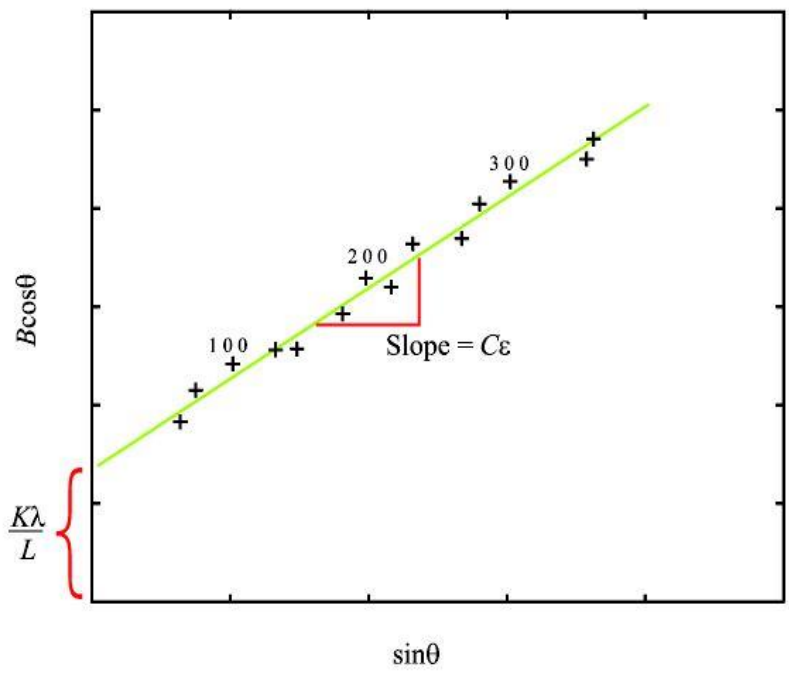

Figure 19 - Example of a Williamson-Hall plot for crystallite size and strain approximation from peak broadening at FWHM[40]

E.2 Scanning electron microscopy

In order to characterize nano/micro-structure, perform elemental analysis, and surface mapping, Field Emission-Scanning Electron Microscopy (FE-SEM) and Energy Dispersive X-Ray Spectroscopy (EDS) equipment are utilized. The FE-SEM has a magnification range of 75 X to approximately 300 kX, and incorporates Smart-SEM user interface software. The magnification range is more than sufficient to analyze fracture surfaces of samples of interest.

The FE-SEM typically operates at 3-5 kV to minimize charging effects and thus collect sharp images. For best resolution, the working distance is 8.5 mm and imaging aperture is

30 µm. Samples are fractured, cleaned, and mounted using carbon tape and an aluminum sample stud. The EDS system employs the same primary e-beam used for SEM imaging, but at an increased spot size and beam current to generate characteristic X-rays from elements in the samples. The incident e-beam interacts with the samples surface causing ejection of an inner-shell electron, decay of an outer-shell electron to fill the vacancy in the inner shell, and emitting a characteristic X-ray that is quantified by the detector . The installed EDS detection system is an Oxford Instruments X-MAX, with Aztec 2.2 SP1 operator interface and image analysis software. Using this system, row 2 elements and higher atomic numbers are analyzed. However, the system has a limitation in spatial resolution of 0.1 micron in the xy plane. Typically, EDS analysis is performed using an emission current of 15-20 keV and an aperture of 60 µm to determine elemental composition of grains, grain boundaries, interfaces, and other micron-scale features, both qualitatively and semi-quantitatively. In this investigation, EDS analysis is used to determine spatial distributions of B, N and Ti after various HPHT treatments [48] [49].

E.3 Transmission electron microscopy

Transmission electron microscopy (TEM) allows phase identification and structural analysis of samples at the submicron-to-nanoscale level. Two microscopes are employed throughout this study: (1) Topcon ABT 002B, and (2) JEOL 2010F TEM/STEM. Bright- and dark-field image analysis enables crystallite size, crystal orientation, and phase boundaries to be determined. High resolution imaging allows direct imaging of atomic lattices, lattice imaging, and study of lattice defects, such as twins and dislocations. In particular, selected area diffraction (SAD) utilizes the diffracted beam to analyze crystal orientation, structure, and degree of crystallinity [50].

E.4 Density measurements

In order to evaluate % theoretical density, also known as relative density, it is necessary to measure the density of the HPHT processed sample using Archimedes' method.

The mass of a dry sample is measured using a high precision analytical balance, and then re-measured when immersed in high purity water. Careful attention is necessary to ensure that no small air bubbles are attached to the sample surface, giving a spurious result. One can use this method to determine the absolute density of a material, compare it to its theoretical density, and arrive at % theoretical density [51].

$$\rho = \frac{m_d}{m_d - m_s}$$

where ρ is absolute density, m is mass of dry sample, and m_s is mass of suspended sample. The % theoretical density is then given by:

$$\% \text{ theoretical density} = (\rho_a/\rho_t) \times 100$$

where ρ_a is absolute density, and ρ_t is theoretical density

E.5 Hardness measurements

Micro-hardness measurements are made using a Leco micro-hardness tester with built-in optical microscope and micrometer stage. A diamond Vickers tip is used, with applied loads of 200g – 1000g. Indent measurements are taken using the built-in microscope and occasionally double-checked using alternative optical or SEM imaging methods. Calibration is done by using a metallic test-block to ensure consistent and repeatable values

are obtained. If a hardness profile is desired, the micrometer stage is typically adjusted to a minimum distance of 3 times the size of the indent. That is, if an indent is 50 µm in diameter, the next indent in the series will usually be placed a minimum of 150 µm away. This is done to ensure that micro-cracking from one indent does not affect the hardness measurements of the next indent in a line profile series [52][53].

The nano-indentation method is used to measure hardness variations across micro-scale distances and features. Measurements are done with a Hysitron Trioboindenter equipped with a diamond Berkovich tip. An electrostatic transducer applies the test loads. The indenter is calibrated with a fused silica standard (E = 68.11 GPa, H = 7.77 GPa) to identify the tip function, and indents are performed in open air before each measurement to account for any position shifting prompted by errant electrostatic forces. Before measurements are taken, it is necessary to map the boundaries of the sample using software controls and a built-in optical microscope for guidance. Indents are measured using the following settings: load control, open-loop indent, trapezoidal or triangular load function, loading rate of 200 µN/sec, and maximum load 1000 µN.

Appendix A presents experimental data, and highlights the challenge of making reliable hardness measurements, due to problems encountered in making smooth surfaces in superhard samples. Invariably, the samples experience grain pull-out during diamond polishing. This problem is still being addressed.

F. Results and Discussion

In this research, significant progress has been made in: (1) HPHT synthesis of cBN powder using Mg as catalyst; (2) HPHT consolidation of laboratory synthesized (and commercially supplied) cBN powder to form nanocrystalline cBN; (3) reactive-HPHT consolidation of mixed cBN/Ti powder to produce Ti-bonded cBN; (4) reactive-HPHT consolidation of mixed hBN/Ti powder to produce Ti-bonded TiB_2/TiN; and (5) reactive-HPHT processing of multi-layered nanocomposite structures, comprising alternating layers of superhard Ti-bonded cBN, hard TiB_2/TiN, and tough Ti. Even so, much remains to be done to lay a firm technical foundation to enable the *scalable processing* of vehicular and personnel armor. To this end, Rutgers/DMI have formed a partnership with a major producer of superhard materials; namely Sandvik Hyperion, formerly Diamond Innovations Inc.

F.1 Synthesis of cBN powder

To synthesize cBN powder, a mixture of hBN and Mg powders is subjected to HPHT processing at 5.0-8.0 GPa/1000-1600°C/5-30 min. The presence of Mg in the powder mixture serves as an activator or catalyst to promote transformation of hBN into cBN under high pressure. The cBN component is extracted from the reaction product by refluxing crushed powder in boiling perchloric acid.

An XRD pattern, ***Figure 20***, of extracted powder indicates an average grain/particle size of about 56 nm. On the other hand, SEM examination of the same powder, ***Figure 21***, shows that the average *particle* size is 1-10 µm. To reconcile these observations, it is reasoned that each micron-sized particle must have a nanocrystalline substructure. Hereafter, this particular cBN powder, produced at DMI, is designated ***Powder #1***.

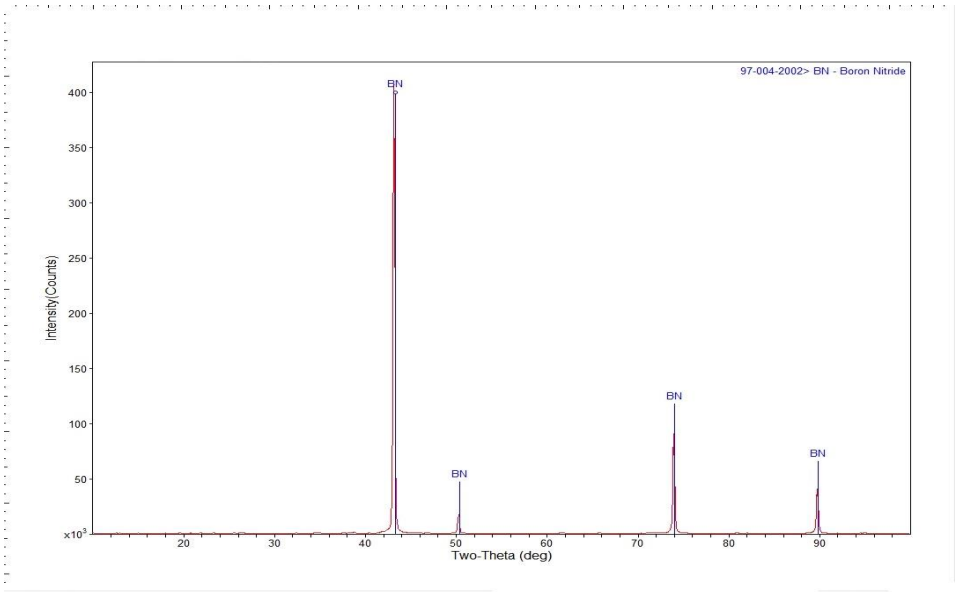

Figure 20 - XRD pattern of powder #1, indicating grain size ~56nm

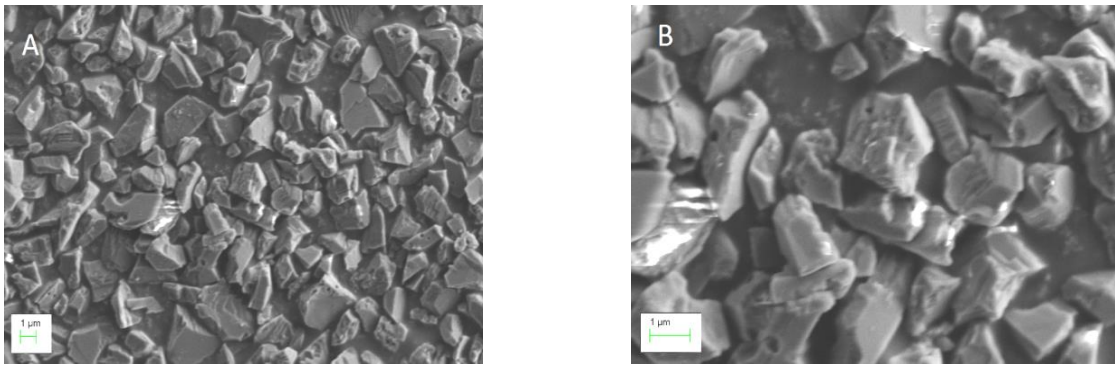

Figure 21 - SEM micrographs of powder #1, showing 1-10 µm particle size.

Another batch of cBN powder, hereafter designated ***Powder #2***, was acquired from Sandvik. In this case, an XRD pattern shows narrow peaks, ***Figure 22***, indicating the absence of a nano-grained substructure, in contrast to Powder #1. Direct observation by SEM, ***Figure 23***, shows that the actual particle size is 50-100 µm. It is noteworthy that all particles in Powder #2 are faceted and have a narrow particle-size distribution. This is a

consequence of the production operation used by the supplier (Sandvik). Relatively large pieces of cBN are crushed into fine powder, thereby creating cleavage facets, and then screened to yield different grades of powder.

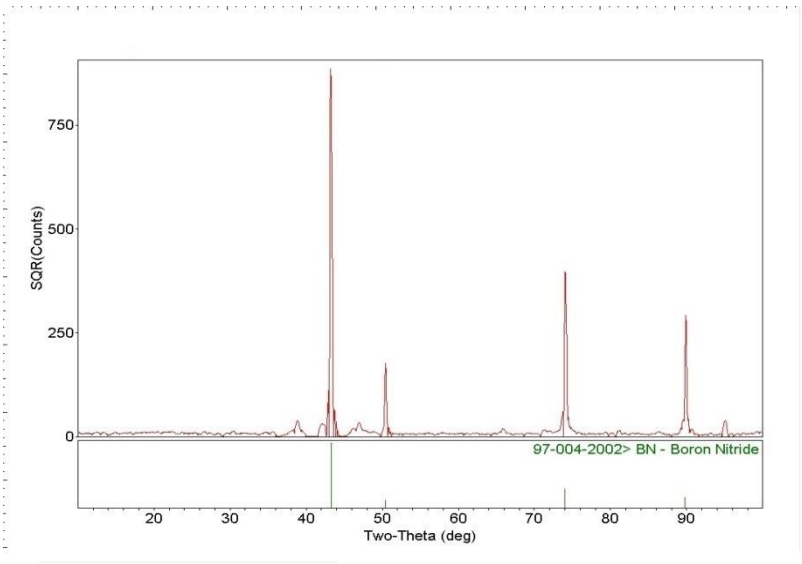

Figure 22 - XRD pattern of powder #2, showing narrow diffraction peaks, indicating coarse grain/particle size.

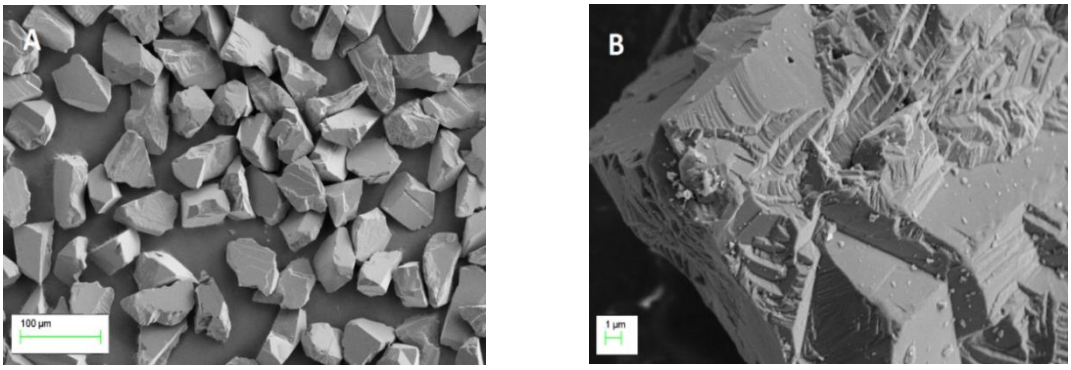

Figure 23 - SEM micrograph of powder #2 50-100 µm particle size and cleavage facets.

F.2 Consolidation of cBN powder

Powder #1

Table 4 presents results for powder #1, after consolidation at 0.3 and 8.0 GPa/1000ºC/15min. All three samples processed at 8.0 GPa are 95-98% density of cBN (ρ = 3.45 g/cm^3), with balance hBN (ρ = 2.1 g/cm^3). The appearance of hBN under such a high pressure is surprising. A possible explanation is that densification via plastic deformation under high pressure is incomplete, forming micro-pores at "triple junctions" between cBN grains, which then become favorable sites for nucleation and growth of the lower density hBN. Such behavior is most likely to occur during heat-up of the sample under high pressure. The larger amount of hBN in the sample processed at 0.3 GPa may be attributed to the same cause. Because of the reduced pressure, densification via plastic deformation is less complete, leaving *larger* micro-pores at triple junctions of cBN that allow more hBN to form.

In all four samples, XRD analysis shows that the crystallite size of the consolidated material is ~30 nm, which is about one-half the initial grain size (~56 nm) of powder #1. Plastic deformation accompanied by recrystallization at points of contact between neighboring cBN particles under high pressure is a possible explanation. However, as noted above, fully dense *phase-pure* cBN is not achievable under the designated processing conditions; a small fraction of hBN is invariably formed. To eliminate cBN decomposition during hot pressing, it will be necessary to investigate the use of sintering aids.

As discussed in section E.3, additions of Ti to cBN prevent its decomposition into hBN, probably by forming a thin surface-passivation film of Ti-base compounds. Moreover, by

controlling reactions between Ti and cBN phases, fully dense composite structures can be obtained, comprising high fractions of *superhard* cBN particles cemented together with *hard* TiB_2/TiN composites. *When such composite structures contain residual un-reacted Ti, there is the prospect of enhanced toughness, while retaining high hardness, stiffness, and strength.*

Table 4 - Summary of results for powder #1, after consolidation at 0.3 and 8.0 GPa/1000ºC/15 min.

						Crystallite Size (nm)		*Volume %*	
Sample ID	*Pressure (GPa)*	*Temp. (ºC)*	*Time (min)*	*Density (g/cm³)*	*% Theoretical density*	*cBN*	*hBN*	*cBN*	*hBN*
Starting Powder #1 (1-10µm particle size)						49	31	99.7	0.33
Exp.1	8.0	1000	15	3.30	95.5	31	49	99.6	0.33
Exp.2	8.0	1000	15	3.30	95.7	32		93.7	
Exp.3	8.0	1000	15	3.41	98.7	33		93.0	
Exp.4	0.3	1000	15	2.75	79.8	33	14	88.6	11.43

Powder #2

Table 5 presents results for powder #2, after consolidation at 8.0 GPa/1000-1900ºC/5-120 min. As indicated, the density increases with temperature in the 1000-1600ºC range, but decreases slightly at 1900ºC. Moreover, there is no significant increase in density with increasing holding time, ranging from 1-120 min at 1000ºC.

Figure 24 presents XRD peak-broadening data, indicating that the average grain size of the material is about 50 nm, and increases slightly with temperature, at least up to 1600ºC, which

Table 5 - Summary of results for powder #2, after consolidation at 0.3 and 8.0 GPa/1000-1900ºC/5-15 min.

						Crystallite Size (nm)		*Volume %*	
Sample ID	*Pressure (GPa)*	*Temp. (ºC)*	*Time (min)*	*Density (g/cm³)*	*Theoretical density (%)*	*cBN*	*hBN*	*cBN*	*hBN*
Starting Powder #2 (50-100µm)						>100		100.0	
Exp.1	**8.0**	1000	15	3.31	95.8	44	19	97.5	2.54
Exp.2	**8.0**	1300	10	3.32	96.3	41	20	98.6	1.36
Exp.3	**8.0**	1600	10	3.37	97.5	52	38	98.7	1.27
Exp.4	**8.0**	1900	5	3.22	93.2	50	23	99.0	0.96
Exp.5	**8.0**	25	45	Not Dense		77		100.0	
Exp.6	**8.0**	1000	1	3.30	95.5	40		100.0	
Exp.7	**8.0**	1000	120	3.30	95.7	28		100.0	
Exp.8	**0.3**	1000	15	2.55	74.0	20	11	28.0	72.0
Exp.9	**8.0**	1600	10	3.34	96.9				
Exp.10	**8.0**	1600	10	3.23	93.7	50	31	99.15	0.85
Exp.11	**8.0**	1600	10	3.37	97.6				

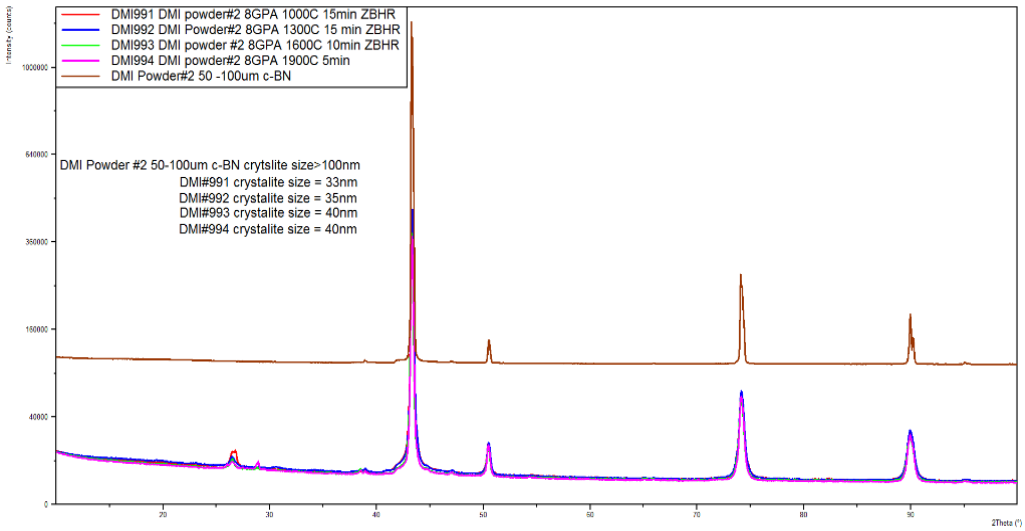

Figure 24 - XRD spectra for powder #2, after processing at 8.0 GPa/1000-1900ºC/5-15 min, showing peak broadening

may be attributed to grain coarsening at higher temperatures. The relatively low intensity peak at $2\theta = 26^{o}$ shows that a small percentage of hBN is present in all samples.

It is noteworthy that powder #2 after HPHT consolidation develops a *nanocrystalline* structure (40-50 nm grain size), even though the original micron-sized (50-100 µm) particles are essentially monocrystalline, with no detectable sub-grain structure. Here again, therefore, it appears that plastic deformation and recrystallization of cBN occurs during powder consolidation, despite its high hardness and strength. Moreover, it seems likely that recrystallization occurs most easily at points of contact between neighboring particles during hot pressing, where Hertzian stresses are most intense. This would explain the relatively large variation in nanocrystalline grain size observed by TEM, as discussed below.

Figure 25 shows SEM images of fracture surfaces for all four samples, showing little or no porosity, in agreement with density measurements. However, their surface morphologies display faceting on a scale comparable to the original particle size (50-100 µm). This is interpreted to be evidence for weakening of the *prior-particle* boundaries by impurities, possibly oxygen in the form of B_2O_3.

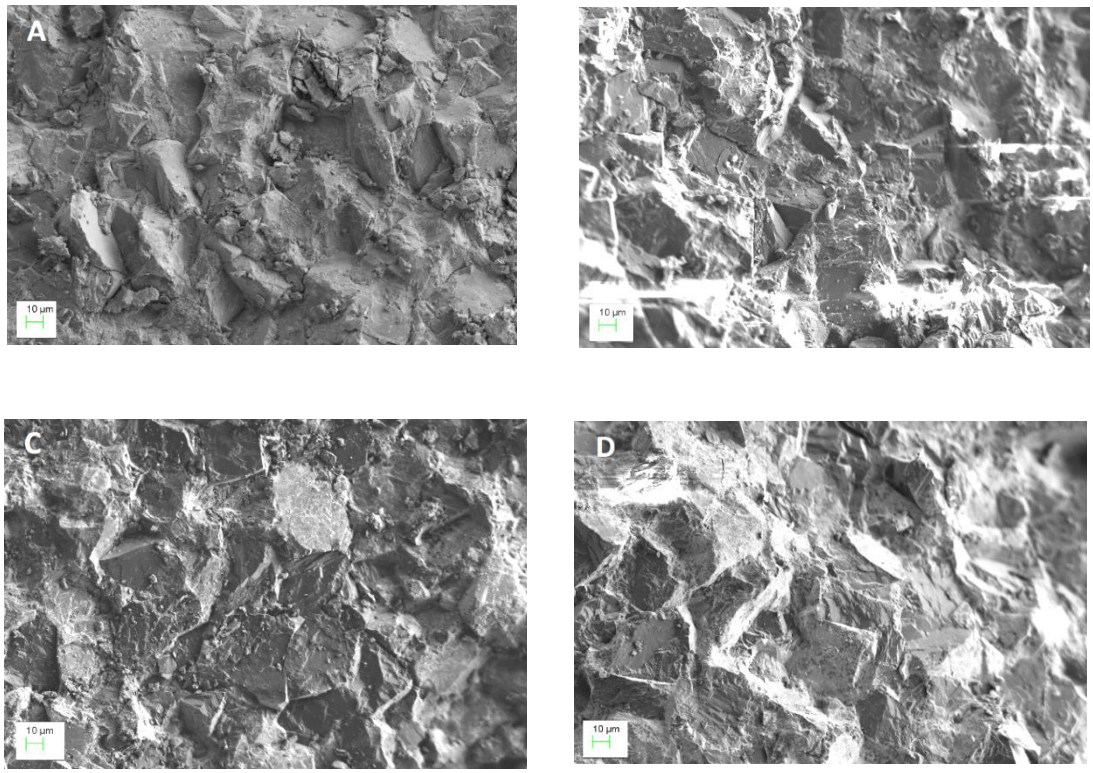

Figure 25 - SEM micrographs of fracture surfaces of c-BN samples, after consolidation at: (a) 1000ºC, (b) 1300ºC, (c) 1600ºC, and (d) 1900ºC, all at 8 GPa.

To obtain a better understanding of the origin of the XRD-peak broadening, ***Figure 24***, one sample was prepared for TEM examination. This was done by crushing the sample to obtain a few fine particles with thin tapered edges suitable for high resolution TEM

observation. ***Figure 26(a)*** shows a nanocrystalline structure, with grain size distribution in the 5-20 nm range, in accord with XRD analysis. The accompanying selected-area diffraction pattern, ***Figure 26(b)***, also shows in addition to continuous rings oval-shaped spots that indicate texturing, which is thought to be the result of preferential alignment of plastically-deformed and partially recrystallized grains under high pressure. In other regions of the same sample, micro-twinning is observed, ***Figure 27***, which has previously been reported only for cBN exposed to very high pressures.

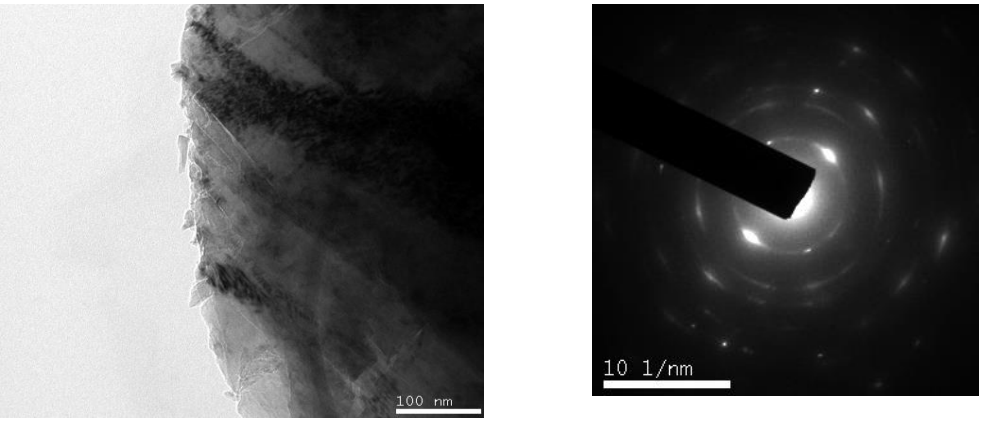

(a) ***(b)***

Figure 26 - TEM micrographs of a c-BN sample, after consolidation at 8 GPa/ 1300ºC/15 min, showing (a) nanocrystalline structure, and (b) evidence for grain texturing.

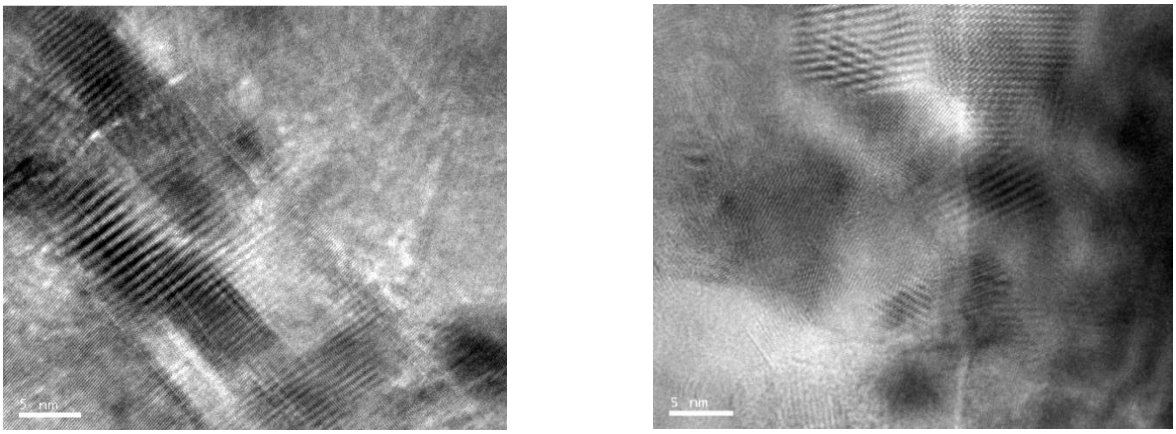

(a) ***(b)***

Figure 27 - TEM micrographs of twinning in a c-BN sample, after consolidation at 8 GPa/ 1300ºC/15 min: (a) single twin ~10 nm in width, and (b) multiple twins ~20 nm in width.

To summarize, fully dense nanocrystalline cBN can be produced by HPHT processing of Powders #1 and 2, but the formation of a minor fraction of hBN seems unavoidable. This is unfortunate, since the presence of even a small amount of hBN, particularly at nano-grain boundaries, must adversely affect fracture toughness. On the other hand, an addition of Ti to cBN provides a route to produce fully dense cBN-base composites without hBN, and thus potentially enhance mechanical performance. On-going research, therefore, is focused on optimizing additions of Ti (and its alloys) to generate a *hard and tough* Ti-base binder for *superhard* cBN particles, preferably with all the constituent phases having nano-scale dimensions. A promising start has been made, as discussed in the following section.

F.3 Consolidation of mixed cBN/Ti powder

A three-step process is used to prepare samples: (1) mechanical mixing of high purity cBN and Ti powders; (2) cold pressing to obtain powder compacts; and (3) consolidation

of compacts via HPHT treatments. Volume % ratios of cBN:Ti are 50:50, 70:30, and 90:10, and HPHT parameters are 0.3, 2.0 and 8.0 GPa/1000ºC/15 min. Under all such processing conditions, chemical reactions occur between cBN and Ti particles, yielding various reaction products.

In what follows, specifics of the HPHT consolidation experiments are described, as well as their micro/nano-structural consequences, and changes in density and hardness. As before, a distinction is made between the behavior of powders #1 and #2 under HPHT processing conditions. All samples are analyzed by XRD, and where appropriate by HR-TEM. For reference purposes, ***Figure 28*** shows standard XRD spectra for several phases of interest herein[54].

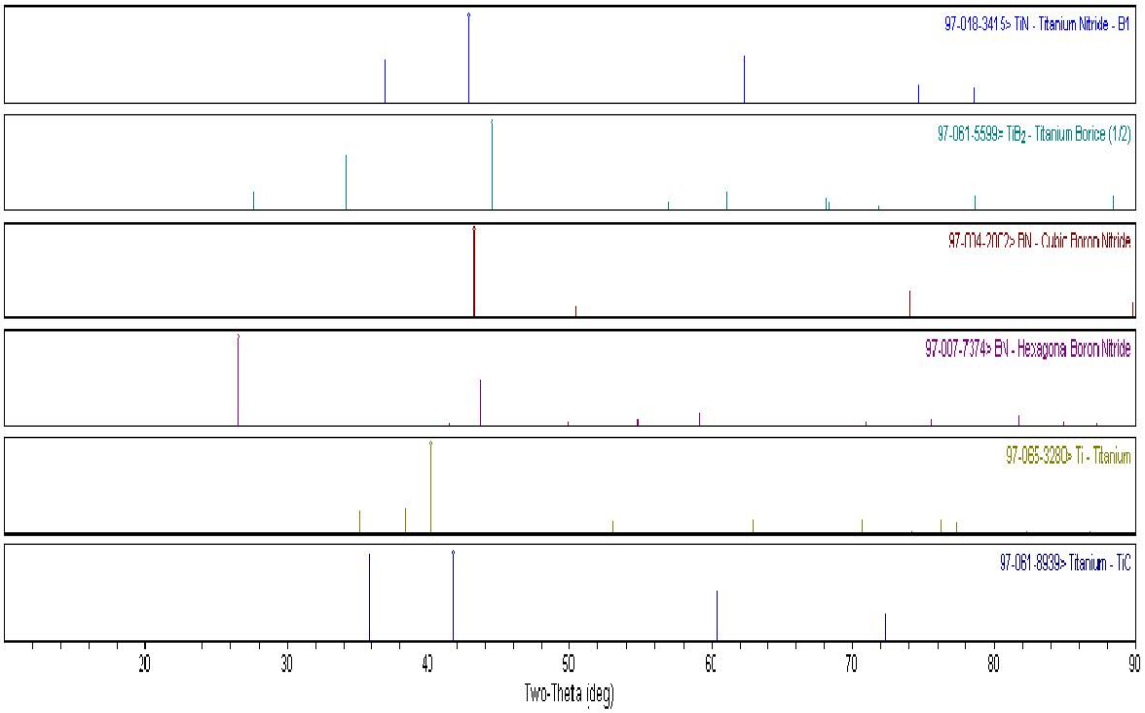

Figure 28 - XRD spectra for cBN, hBN, Ti, TiN, TiB_2, and TiC from ICSD files

Powder #1 + Ti

Table 6 summarizes results of density measurements for samples with 50:50, 70:30 and 90:10 cBN:Ti compositions, after consolidation at 0.3, 2.0, and 8.0 GPa/1000ºC/15min. At 8.0 GPa, all three samples have densities 94-96% theoretical, whereas at 0.3 GPa and 2.00 GPa, densities are lower and display greater variability. For example, the 90:10 sample processed at 0.3 GPa has a density of only 74%. These differences in density reflect different degrees of *reaction between cBN and Ti particles* during HPHT processing, as will now be shown.

Table 6 - Densities of cBN:Ti samples, after consolidation at 0.3, 2.0, and 8.0 GPa/1000ºC/15min.

Sample ID	*cBN:Ti ratio (vol.%)*	*Pressure (GPa)*	*Temp. (ºC)*	*Time (min)*	*Density (g/cm^3)*	*% Theoretical density*
Exp.1	50:50	**8.0**	1000	15	3.73	93.7
Exp.2	70:30	**8.0**	1000	15	3.84	95.9
Exp.3	90:10	**8.0**	1000	15	3.45	95.7
Exp.4	50:50	**2.0**	1000	15	3.69	92.8
Exp.5	70:30	**2.0**	1000	15	3.38	89.3
Exp.6	90:10	**2.0**	1000	15	3.03	84.3
Exp.7	50:50	**0.3**	1000	15	3.78	94.9
Exp.8	70:30	**0.3**	1000	15	3.04	80.2
Exp.9	90:10	**0.3**	1000	15	2.68	74.4

Table 7 - XRD phase analysis of cBN:Ti samples, after consolidation at 0.3, 2.0, and 8.0 GPa/1000ºC/0,3,&15min.

Sample ID	*cBN:Ti ratio (vol. %)*	*Pressure (GPa)*	*% cBN*	*% hBN*	*% Ti*	*% TiN*	*% TiB_2*
Exp. 1	50:50	**8.0**	40.1	4.2	55.8	-	-
Exp. 2	70:30	**8.0**	63.3	2.0	34.7	-	-
Exp. 3	90:10	**8.0**	90.4	-	9.6	-	-
Exp. 4	50:50	**2.0**	42.7	-	50.9	6.4	-
Exp. 5	70:30	**2.0**	73.0	-	20.1	6.9	-
Exp. 6	90:10	**2.0**	93.2	-	6.8	-	-
Exp. 7	50:50	**0.3**	33.6	-	-	31.5	34.9
Exp. 8	70:30	**0.3**	67.5	-	-	15.4	17.1
Exp. 9	90:10	**0.3**	67.2	-	-	7.9	5.0

Table 7 summarizes *qualitative* XRD data for the consolidated samples. Processing of *50:50 mixtures* of cBN:Ti powders at 0.3, 2.0 and 8.0 GPa yields three distinct products, depending on the *applied pressure*. At *8.0 GPa*, there is no detectable reaction with Ti for all three cBN:Ti compositions. Since their measured densities are close to theoretical, taking into account different concentrations of higher density Ti (4.51 g/cm^3) in the starting mixtures, it is concluded that all three compositions are Ti-bonded cBN composites. In agreement with this conclusion, ***Figure 29*** shows evidence for extensive plastic deformation of the original Ti particles under high pressure, apparently filling the open porosity in the original cBN:Ti powder compact.

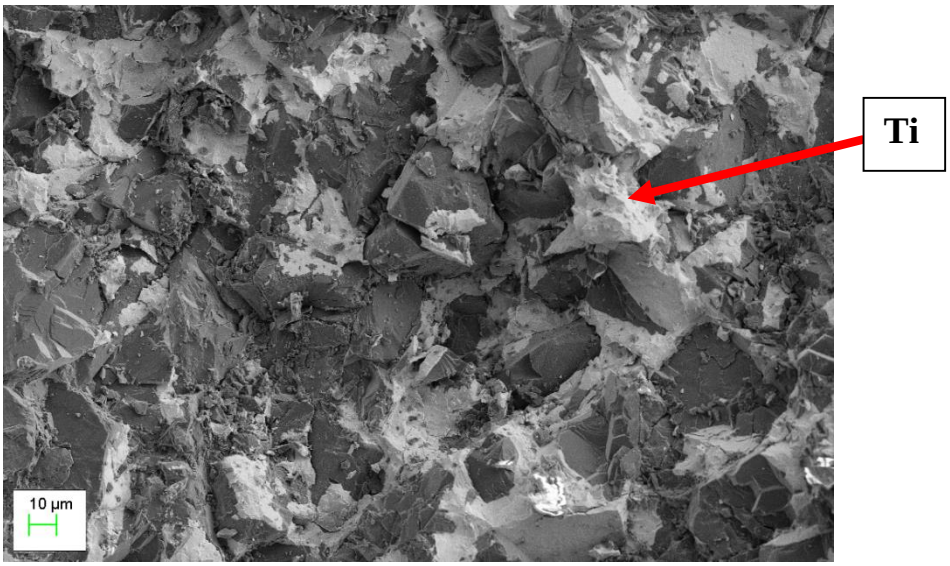

Figure 29 - SEM image of 50:50 cBN/Ti, after consolidation at 8.0 GPa/1000ºC/15 min

In striking contrast, when the same powder compacts are consolidated at *0.3 GPa*, the resulting composites consist of cBN, TiB_2 and TiN, *but no crystalline Ti*. In this case, cBN and Ti particles react to form TiB_2/TiN-bonded cBN composites, with varying amounts of reactants, depending on the starting compositions. On the other hand, at *2.0 GPa*, reactions between Ti and cBN particles are incomplete, resulting in various mixtures of c-BN, TiN and Ti, but *no* TiB_2. All three compositions show similar behavior in that percentages of TiN and TB_2 reaction products decrease in direct proportion to the amount of Ti in the cBN:Ti starting mixtures. It is noteworthy that at 2.0 GPa, the absence of TiB_2 and smaller amounts of TiN occur for all three cBN:Ti starting compositions.

Figure 30 shows XRD spectra for 50:50 mixtures of cBN:Ti, after consolidation at 0.3, 2.0 and 8.0 GPa/1000ºC/15 min. The broad XRD diffraction peaks displayed by TiB_2 and TiN phases indicate that the average particle size for both phases is <20 nm, whereas that

for the un-reacted c-BN component is about the same as the starting powder (1-10 µm). High resolution TEM analysis confirms the presence of TiB_2 and TiN nanophases, and micron-sized c-BN particles. Even so, the average particle size for both reactant phases varies from one region to the next. Dark-field observations using different locations on the diffraction rings show uniformity in mixing of the two nanophases, with average particle size ~5 nm. Imaging using spotty rings also shows a uniform duplex-phase distribution, with average particle size ~20 nm. Area-scans and line-profile EDS analyses show that concentrations of B and N in both c-BN and TiB_2/TiN regions are comparable, as would be expected for reaction of Ti with elementally-mixed B and N in the original c-BN particles. *Such structural uniformity in a ceramic nanocomposite would be difficult to achieve via conventional mixing and consolidation of nanopowders. Hence, this new approach to synthesizing ceramic nanocomposites is considered to be a singular contribution of the present research.* But, of course, further research is needed to fully understand and document mechanism and kinetics of co-nucleation of the constituent ceramic phases, and their subsequent growth.

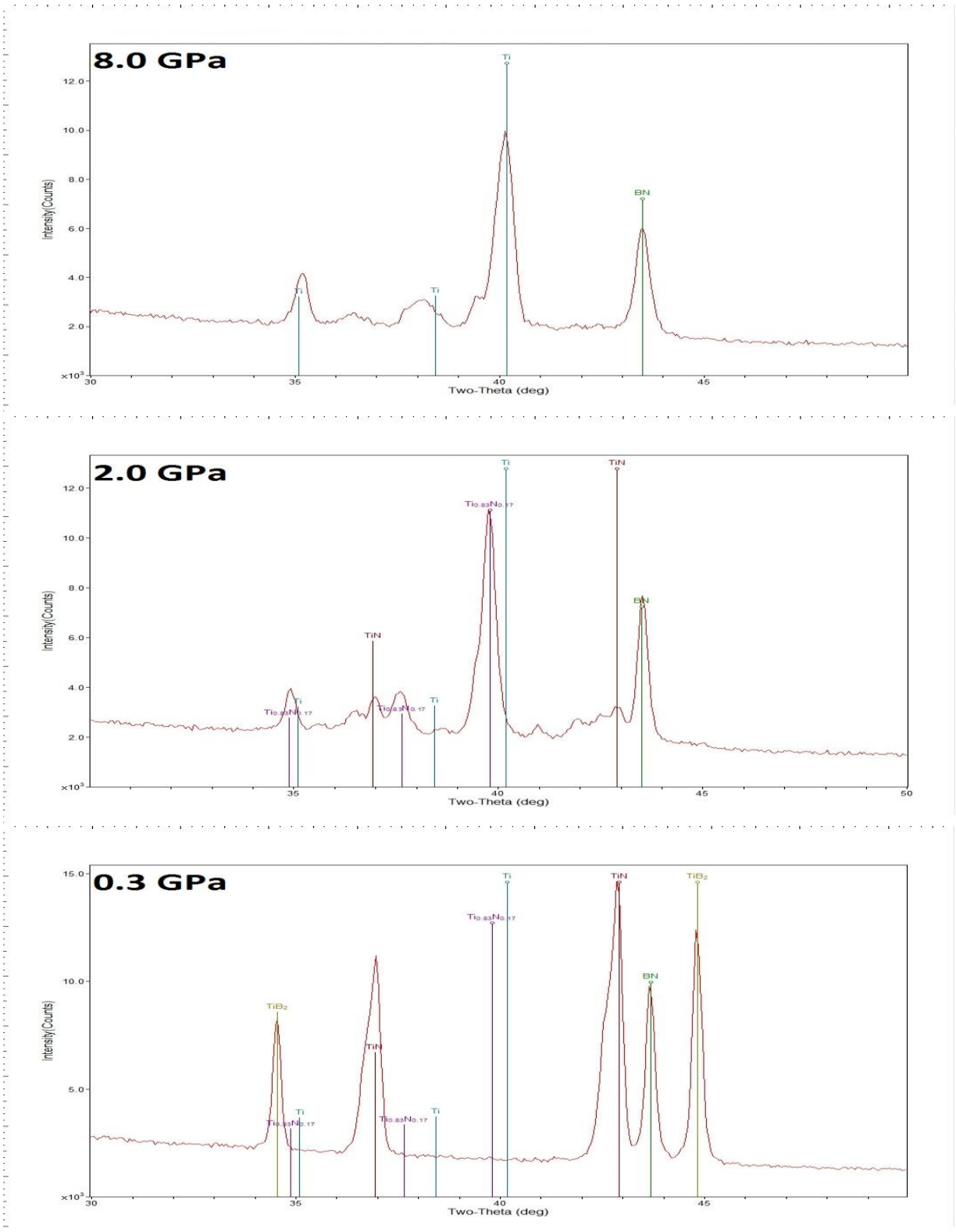

Figure 30 - XRD spectra for 50:50 cBN:Ti, after consolidation at 0.3, 2.0 and 8.0 GPa/1000ºC/15 min.

Similar XRD spectra are obtained for all samples, with the intensities of the main diffraction peaks correlating with the starting powder compositions. For example, 50:50, 70:30 and 90:10 powder mixtures, after consolidation at 8.0 GPa, show corresponding reductions of Ti in the resulting cBN:Ti nanocomposites. Similarly, at 0.3 GPa, the amounts of reaction products (TiB_2 and TiN phases) in the consolidated samples decrease proportionally with Ti content in the starting powder mixtures.

The 90:10 nanostructured composite is noteworthy, in that it contains the largest fraction of *superhard* cBN, with no evidence for soft hBN, and the smallest fraction of *hard* TiB_2/Ti binder phase, thus offering potentially the highest hardness and stiffness. In the event that improved toughness is required, this may be accomplished by reducing the holding time during HPHT processing, so as to leave some fraction of un-reacted Ti in the TiB_2/TiN-bonded cBN nanocomposite. This possibility will be investigated in future work, guided by the results summarized in **Tables 6 and 7**.

For a 70:30 cBN:Ti powder mixture, consolidated at 2.0 GPa/1000ºC/15 min, the resulting composite shows all the peaks expected for cBN, Ti and TiN, ***Figure 31***, but there are no peaks for TiB_2. However, there are two additional broad peaks (arrows) that indicate the presence of another phase. Since the peaks are shifted to smaller angles (larger d-spacings) relative to Ti, this suggests the presence of an intermediate phase, i.e. a precursor to TiB_2 formation. This being the case, an appropriate post-annealing treatment should induce precipitation of nanophase TiB_2, thereby forming a nanocomposite similar to that formed directly via reaction synthesis at 0.3 GPa. However, specifics of the reaction mechanisms involving dual-phase nucleation and subsequent growth are not yet understood. Wreidt et al. saw similar peak shifting to larger 2θ angle positions as the lattice

constant shrank, this occurred due to increasing N above stoichiometric TiN[55]. In the course of these experiments as a predecessor to TiB_2 formation, the converse is observed as the lattice parameter is expanding and the peak is shifting to lower 2θ angles.

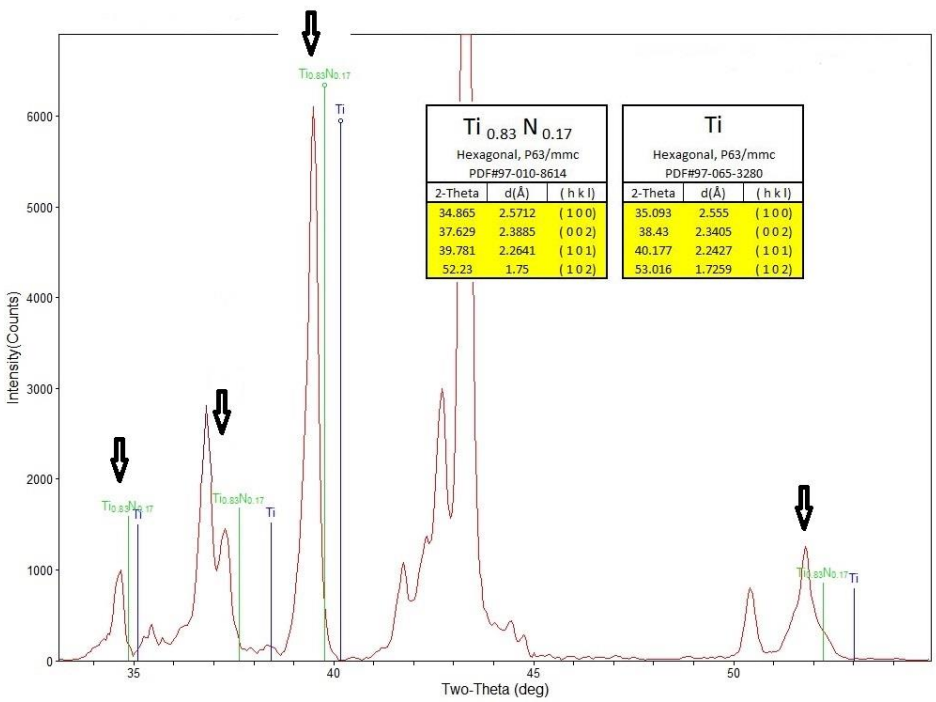

Figure 31 - XRD spectra for 70:30 cBN:Ti, after consolidation at 2.0 GPa/1000ºC/15 min, showing evidence for intermediate-phase formation (arrows)

<u>Powder #2 + Ti</u>

Table 8 summarizes results of density measurements for samples with 50:50, 70:30 and 90:10 cBN:Ti compositions, after consolidation at 0.3, 2.0, and 8.0 GPa/1000ºC/15min. Under all HPHT processing conditions, densities are higher than that of ***Table 6.*** Thus, the evidence is clear, powder #2 (industrial-grade cBN powder, 50-100 µm particle size) yields

higher density products than powder #1 (laboratory-grade cBN powder, 1-5 µm particle size). This difference in behavior is attributed to the higher quality of the *industrial-grade* powder (dense monocrystalline particles), which enables surface reaction between cBN and Ti particles to form a dense Ti-bonded cBN composite at 8.0 GPa or a dense TiB_2/TiN-bonded cBN composite at 0.3 GPa. In contrast, the *laboratory-grade* powder (porous nanoparticle aggregates) restricts reaction of Ti within the nanoparticle aggregates, resulting in incompletely densified samples. In both cases, it is plastic deformation of the Ti particles under high pressure that fills all easily accessible pore space in the powder compact, thus facilitating reaction between cBN and Ti.

Such reactions, summarized in ***Table 9***, are initiated at surface areas of contact between cBN and Ti particles. At 8.0 GPa a *Ti-bonded cBN composite* is formed, whereas at 0.3 GPa a *TiB_2/TiN-bonded cBN* composite is formed; 2.0 GPa is an intermediate case where reaction is incomplete. At 0.3 GPa, in all three cases, the resulting composite consists of a high fraction of un-reacted cBN particles in a TiB_2/TiN nanocomposite matrix. It is noteworthy, that the highest density TiB_2/TiN-bonded cBN composite occurs for a 50:50 cBN:Ti composition *processed at 0.3 GPa/1000ºC/15min.* Under such processing conditions, it is entirely feasible that process scaling can be accomplished using *conventional hot isostatic pressing (HIP) and vacuum sinter-HIP technologies.*

An important point is the *absence* of hBN phase in retained cBN at 0.3 GPa, since any amount of this phase that decorates grain boundaries should degrade mechanical properties, particularly fracture toughness. By eliminating this phase, therefore, effective load transfer between superhard (cBN) particles and hard TiB_2/TiN matrix can be achieved, as required for composite strengthening. Samples processed at 0.3 GPa also react with the graphitic-

carbon heater, ***Table 9***, forming a *thin* layer of TiC; its absence in samples processed at 2.0 GP and 8.0 GPa is not understood.

As discussed below, a strong exothermic reaction between cBN and Ti particles during HPHT processing contributes to the effectiveness of the consolidation process particularly at low temperatures. Work is underway to determine the lowest consolidation temperature to produce a TiB_2/TiN-bonded cBN composite that combines high specific strength and stiffness with superior fracture toughness.

Table 8 - Densities of cBN:Ti samples, after consolidation at 0.3, 2.0, and 8.0 GPa/1000ºC/15,3,0 min.

Sample ID	*cBN:Ti ratio (vol.%)*	*Pressure (GPa)*	*Temp.(º C)*	*Time (min)*	*Density (g/cm³)*	*% Theoretical density*
Exp.1	50:50	**8.0**	1000	15	3.92	98.6
Exp.2	70:30	**8.0**	1000	15	-	-
Exp.3	90:10	**8.0**	1000	15	-	-
Exp.4	50:50	**2.0**	1000	15	3.79	95.3
Exp.5	70:30	**2.0**	1000	15	3.42	90.3
Exp.6	90:10	**2.0**	1000	15	3.38	93.9
Exp.7	50:50	**0.3**	1000	15	3.98	100.2
Exp.8	50:50	**0.3**	1000	0	3.87	97.11
Exp.9	70:30	**0.3**	1000	15	3.68	97.2
Exp.10	90:10	**0.3**	1000	15	3.03	84.1
Exp.11	50:50	**0.1**	900	3	3.96	99.5

Table 9 - XRD phase analysis of cBN:Ti samples, after consolidation at 0.3, 2.0, and 8.0 GPa/1000ºC/15min.

Sample ID	*cBN:Ti ratio (vol. %)*	*Pressure (GPa)*	*% cBN*	*% hBN*	*% Ti*	*% TiN*	*% TiB_2*	*% TiC*	*% $Ti_{0.83}N_{0.17}$*	*% TiB*
Exp. 1	50:50	8	65.70	2.64	30.80	-	-	-	-	-
Exp. 2	70:30	8	74.05	3.40	21.37	-	-	-	-	-
Exp. 3	90:10	8	94.17	0.80	5.03	-	-	-	-	-
Exp. 4	50:50	2	77.86	1.83	20.31	-	-	-	-	-
Exp. 5	70:30	2	83.17	2.16	14.67	-	-	-	-	-
Exp. 6	90:10	2	91.70	4.14	4.16	-	-	-	-	-
Exp. 7	50:50	0.3	72.81	-	-	14.44	3.44	4.83	1.15	-
Exp. 8	50:50	0.3	51.7	34.64	-	2.70	-	-	9.88	1.01
Exp. 9	70:30	0.3	84.83	-	-	7.36	7.81	-	-	-
Exp. 10	90:10	0.3	92.29	-	-	2.62	2.85	2.24	-	-
Exp. 11	50:50	0.1	78.13	1.78	-	11.62	-	-	6.76	1.72

F.4 Consolidation of mixed hBN/Ti powder

The effects of HPHT consolidation of hBN/Ti powder is expected to be similar to that for cBN/Ti powder. In fact, this is shown to be the case, at least for hBN:Ti 50:50 and 30:70 compositions, after HPHT processing at 0.3, 2.0 and 8.0 GPa/1000ºC/15-120 min.

Figure 32 compares SEM micrographs for a 30:70 hBN:Ti powder mixture, after consolidation at 0.3 GPa for *15 and 120 min*. Evidently, the amount of hBN phase (dark-contrast) is decreasing with increasing holding time. ***Tables 10 and 11*** also show that increasing the holding time increases the degree of reaction between hBN and Ti, forming

not only larger amounts of TiB_2 and TiN, but also TiB and TiN_2. In both cases, there is no residual un-reacted Ti, so that its conversion to Ti-base phases via reaction with hBN is essentially complete. The relatively high density of the consolidated materials also reflects conversion of hBN (ρ = 2.1 g/cm^3) into higher density (ρ = 4.5-4.7 g/cm^3) Ti-base phases. The 50:50 hBN:Ti composition is an intermediate case, where there is less Ti available *initially* for reaction with hBN, thus yielding smaller amounts of TiB_2 and TiN phases and a lower density.

Figure 33 shows an EDS map of a 30:70 hBN:Ti sample, after processing at 0.3 GPa/1000ºC/*120 min*. The observed distribution of B, N, and Ti confirms that the composite consists of coarse hBN particles dispersed in a fine-scale TiB_2/TiN composite matrix.

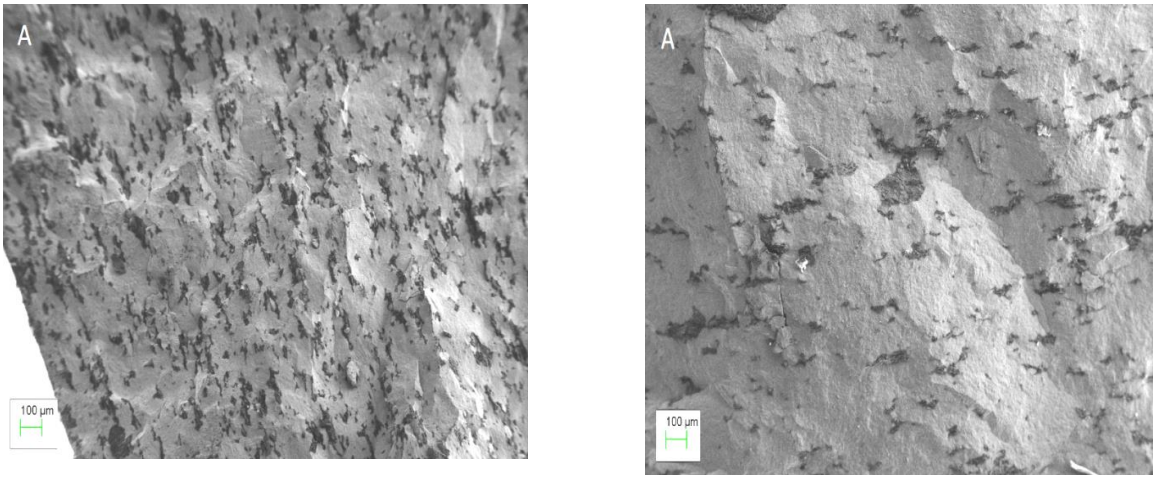

(a) ***(b)***

Figure 32 - SEM images of 30:70 hBN:Ti after consolidation at 0.3 GPa/1000ºC: (a) 15 min and (b) 120 min, showing smaller fraction of hBN particles (dark contrast) with longer holding time.

Table 10 - Densities of hBN:Ti samples, after consolidation at 0.1, 0.3, 2.0, and 8.0 GPa/1000ºC, showing high density of fully reacted material.

Sample ID	hBN:Ti ratio (vol.%)	Pressure (GPa)	Time (min)	Temp. (ºC)	Density (g/cm^3)	% Theoretical density
Exp.1	50:50	**8.0**	15	1000	3.26	96.5
Exp.2	50:50	**2.0**	15	1000	3.53	104.4
Exp.3	50:50	**0.3**	15	1000	4.03	119.3
Exp.4	50:50	**0.3**	0	1000	3.967	117.5
Exp.5	50:50	**0.1**	15	1000	4.031	119.4
Exp.6	33:67	**0.3**	15	1000	4.50	119.6
Exp.7	33:67	**0.3**	120	1000	4.71	125.4

Table 11 - XRD phase analysis of hBN:Ti samples, after consolidation at 0.3, 2.0, and 8.0GPa/1000ºC.

Sample ID	hBN:Ti ratio (vol. %)	Pressure (GPa)	Time (min)	% cBN	% hBN	% Ti	% TiC	% TiN	% TiB_2	% TiB	% Ti_2N
Exp. 1	50:50	**8.0**	15	-	75.44	21.56	3.10	-	-	-	-
Exp. 2	50:50	**2.0**	15	-	67.88	28.56	4.47	-	-	-	-
Exp. 3	50:50	**0.3**	15	-	53.64	-	4.57	29.02	12.78	-	-
Exp. 4	50:50	**0.3**	0	-	64.72	-	-	3.77	27.73	2.79	-
Exp. 5	50:50	**0.1**	15	-	52.34	-	-	10.96	35.58	1.125	-
Exp. 6	33:67	**0.3**	15	-	31.93	-	-	42.07	8.70	8.15	9.15
Exp. 7	33:67	**0.3**	120	-	15.74	-	-	58.90	18.73	5.73	0.90

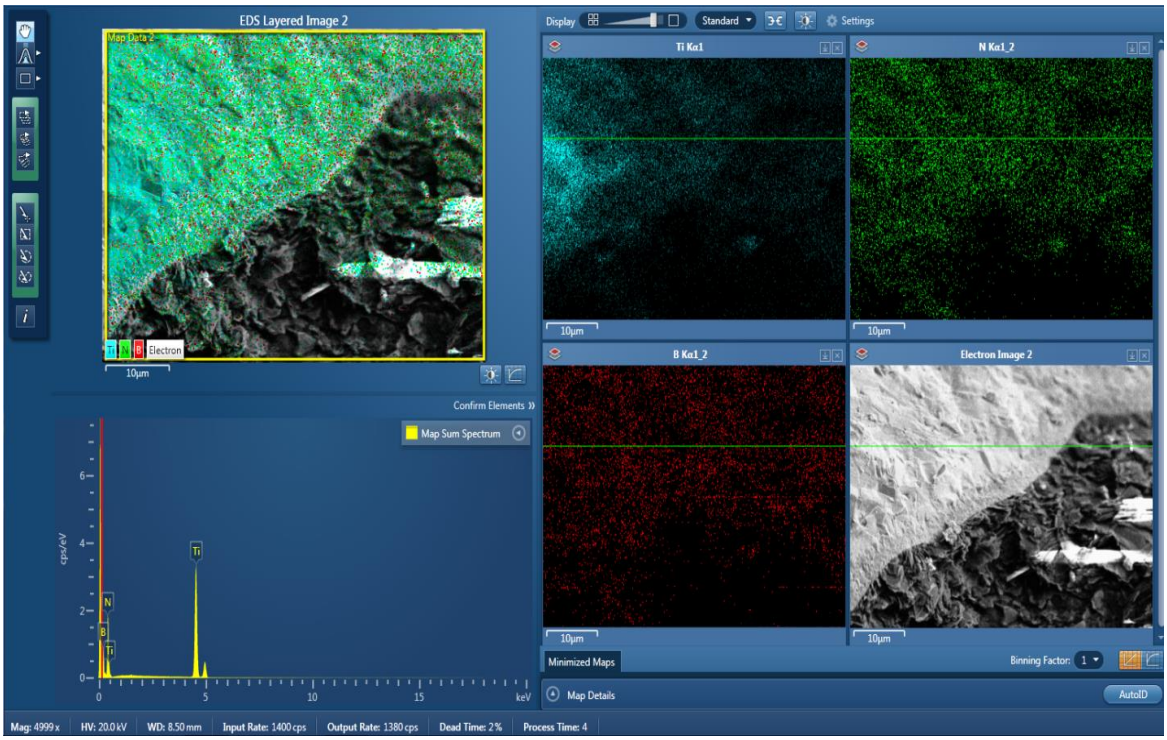

Figure 33 - EDS map of 30:70 hBN:Ti sample, after processing at 0.3 GPa/1000ºC/15min, showing presence of B and N in the Ti-rich matrix phase.

F.5 Consolidation of multi-layered structures

It has been shown that, depending on the HPHT processing parameters adopted, mixtures of cBN/Ti and hBN/Ti powders react exothermically to form a wide range of nanocomposite structures. A cBN/Ti powder mixture transforms into a *superhard* cBN-base composite, consisting of a high fraction of *superhard* cBN particles in a *hard* TiB_2/TiN nanocomposite matrix or binder phase. On the other hand, a hBN/Ti powder mixture transforms into a *hard* TiB_2/TiN. In both cases, compositions and processing parameters can be adjusted to yield residual un-reacted Ti for improved toughness.

This ability to react h-BN and c-BN with Ti to produce hard and superhard nanocomposites, often under the same HPHT processing conditions, enables multi-layered

structures to be fabricated in a one-step operation. *In principle, such structures may be designed to satisfy shock-impedance mismatch and shock-wave dispersion requirements for high performance armor, and possibly provide a multi-hit capability*.

Two attempts are made to fabricate layered-composite structures, comprising alternating layers of *hard* and *superhard* phases, with interlayers of *soft* Ti. In the first experiment, a 7-layer powder compact of cBN and Ti is consolidated at 0.3 GPa/750°C/15min. The consolidated sample shows delamination at interphase interfaces, probably due to thermal-expansion and elastic-modulus misfit stresses that develop between the different layers. Because of the complexity of the structure observed, no further work is planned on this material. To simplify matters, in the second experiment, a 2-layer powder compact is consolidated under the same HPHT conditions. The powder compact (9.5 mm dia x 5 mm), ***Figure 34,*** consists of a top layer (4-mm thick) of 70:30 TiC:Ti and a bottom layer (1-mm thick) of 50:50 cBN:TiC/Ti.

After HPHT consolidation at 0.3 GPa/750°C/15min, a monolithic sample of high density (ρ = 4.79 g/cm^3) is realized. The top layer reacts with the graphitic-carbon heater to form a thin layer of TiC, with no evidence for residual un-reacted Ti, ***Figure 35(a)***. On the other hand, the bottom layer reacts with the graphitic-carbon heater to form a composite structure, comprising about 75% cBN, 24% TiC, and 1% of Ti, ***Figure 35(b)***. This result is similar to that of previous experiments at pressures of 0.3 GPa, where Ti stabilizes the cBN and prevents its surface decomposition into hBN. The possibility that a thin passivation film of TiB_2/TiN forms on the cBN particle surfaces, preventing further reaction with Ti, is being investigated.

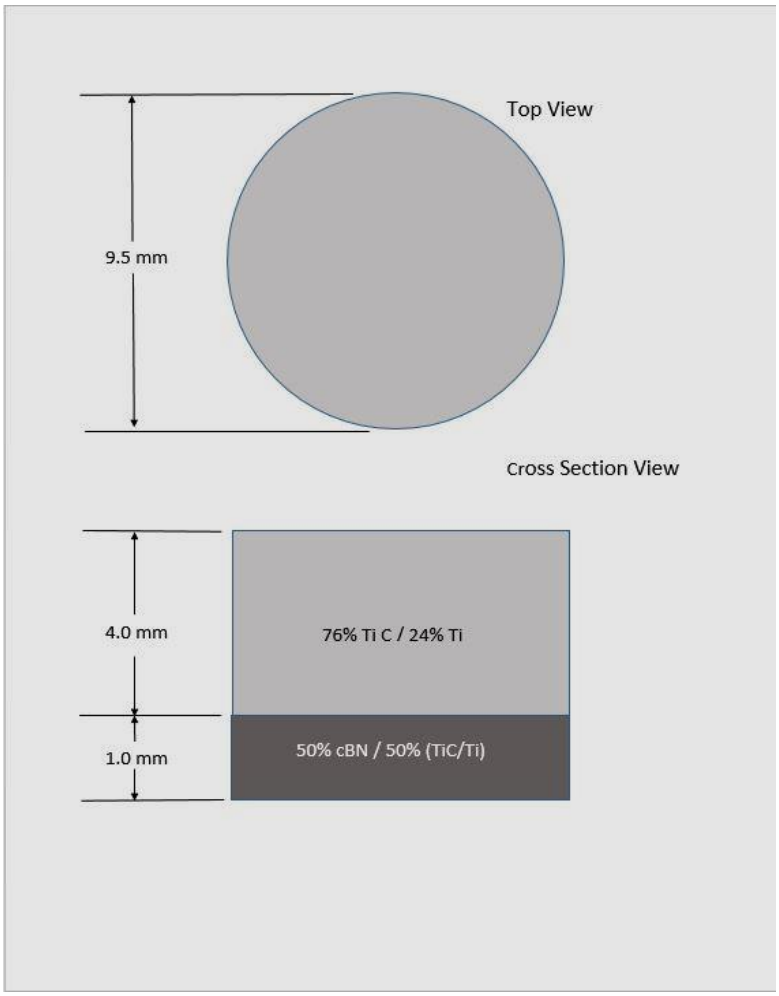

Figure 34 - Schematic of a bi-layered composite sample, showing thickness of each layer and its composition.

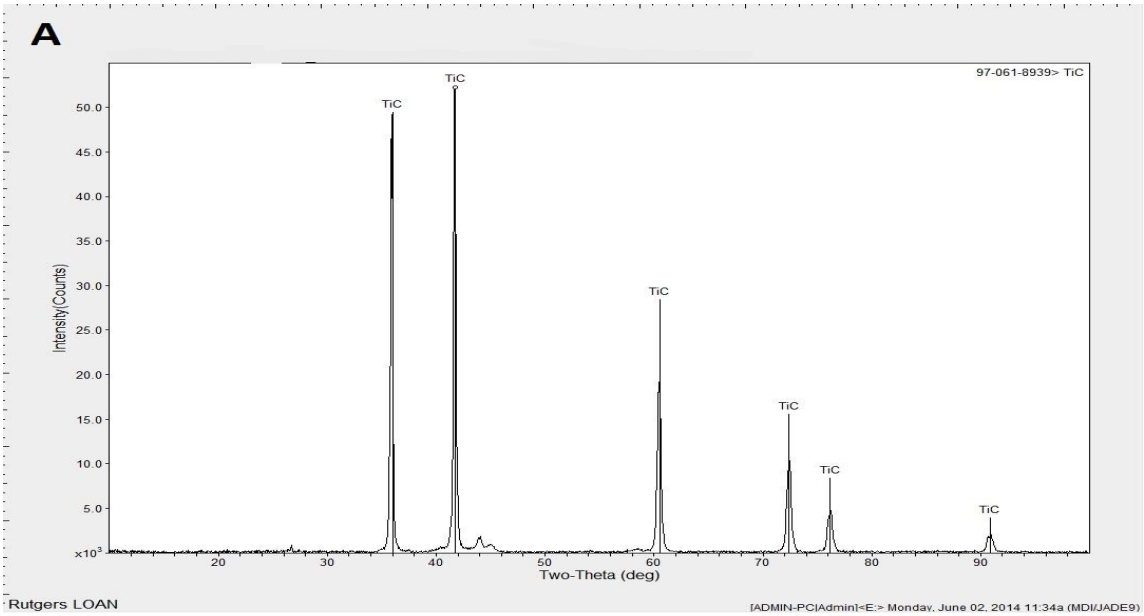

(a)

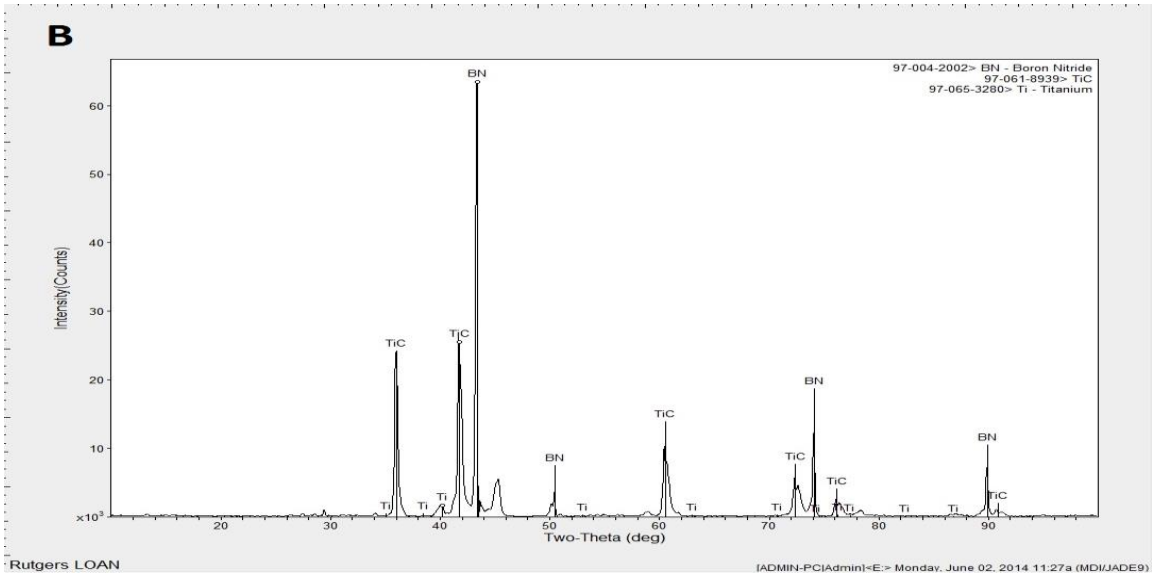

(b)

Figure 35 - XRD spectra of a bi-layered composite sample, showing (a) TiC in its top layer, and (b) cBN/TiC in its bottom layer.

It is noteworthy that in all experiments under *reduced* high pressure conditions, including the above, the pressure requirements for processing Ti-bonded c-BN, Ti-bonded TiB_2/TiN, and layered structures are as low as 0.3 GPa, and possibly lower, so that scalability is not an issue. In fact, it appears that conventional hot-isostatic pressing (HIP) and sinter-HIP technologies can be used to produce ceramic armor plates of any desired size and shape.

G. Discussion

The synthesis of materials by exploiting exothermic reactions, called "combustion synthesis", continues to engage the interest of academic and industrial researchers, since it is a cost-effective and scalable method to produce refractory materials, ceramics, composites and intermetallic compounds[56-65]. Combustion synthesis methods can be broadly classified into two main types: (1) *bulk synthesis*, where a well-mixed powder compact of reactants is ignited by raising the temperature to the ignition point, such that the entire compact experiences a very fast massive transformation to the final product; and (2) *self-propagating synthesis*, where reaction is initiated at some point in a powder compact, and then propagates as a combustion wave throughout the compact, driven by an exothermic reaction at its leading edge. The latter is called self-propagating high-temperature synthesis (SHS). Under such processing conditions, the adiabatic reaction temperature is high (5000 K), wave-propagation rate rapid (25 cm/s), thermal gradient steep (10^5 K/cm), and cooling rate fast (10^5 K/s). Thus, far-from-equilibrium or metastable phases are attainable, such as extended-solid solution, metastable intermediate, and amorphous phases, as well as nanocrystalline (one component) and nanocomposite (two or more components) materials. Even so, the resulting products are quite porous, typically about 50% of theoretical density, so that further processing is needed to achieve complete densification. Similar SHS-based methods are also used to fabricate bulk materials via solid-solid or solid-gas reactions, and coatings by thermal spraying[66-70].

When dealing with powder processing, pressure-assisted SHS is favored, since the final densified product is obtained directly by combining powder synthesis and consolidation in a single operation. The method described herein, called *reactive-HPHT synthesis*, is one

such method, since reaction between the constituent phases in a well-mixed powder compact is performed under a sustained pressure at high temperature, thus ensuring a pore-free product. *A feature of the process is its ability to transform the same starting powder composition into different products by varying reaction pressure at a fixed reaction temperature or vice versa*. For example, reactive-HPHT processing of a 50:50 composition of cBN:Ti powder at 0.3, 2.0 and 8.0 GPa/1000ºC/15 min yields three distinct composite products. At *8.0 GPa*, no detectable reaction of cBN with Ti occurs, resulting in a *Ti-bonded cBN* composite. In striking contrast, at *0.3 GPa*, complete reaction between cBN and Ti occurs, resulting in a *TiB_2/TiN-bonded cBN* composite. On the other hand, at *2.0 GPa*, reaction between Ti and cBN is incomplete, resulting in a *Ti/TiN-bonded c-BN* composite with no detectable TiB_2. Similar reactions occur for other compositions and for different starting materials, e.g. hBN instead of cBN. Since reaction between Ti and BN is exothermic, reaction (1) below, the thermal transient generated during processing, irrespective of reaction mode (bulk or self-propagating), facilitates pressure-assisted sintering to full density, while achieving an ultrafine-grained structure due to the rapid self-quenching experienced by the consolidated product.

$$2BN + 3Ti \rightarrow TiB_2 + 2TiN \quad (\Delta H = -467 \text{ kJ/mol}) \qquad (1)$$

In the procedure adopted for reactive-HPHT processing of Ti with BN, after the application of high pressure to a mixed-powder compact at ambient temperature, the compact is heated to 1000ºC and held at this temperature for 15 min. Of particular interest is the effect on reaction kinetics of the s*cale of particle mixing* in the initial powder compact. Initial results indicate that fine-scale mixing of the reactants causes very rapid conversion, even detonation, resulting in an ultra-fine or nanostructured composite; such

is not the case for coarse-scale mixing of the reactants, where time-dependent reaction processing is observed. According to reaction (1), 2 mol of TiN are generated for every 1 mol of TiB_2, which corresponds to about a 70:30 ratio of the two phases. At this ratio, a bicontinuous nanocomposite is formed in which the constituent nanophases are interpenetrating in three dimensions. Such a composite structure is known to resist coarsening at high temperature, so that a host of high-temperature applications are conceivable, such as heat/corrosion-resistant ceramics for gas-turbine and rocket engines.

An addition of *more* cBN than is required to complete reaction (1) yields a dispersion of un-reacted cBN particles in a TiB_2/TiN matrix, reaction (2), whereas an addition of *more* Ti than required to complete reaction (1) yields a dispersion of un-reacted Ti particles in a TiB_2/TiN matrix, reaction (3). Both types of composites have their potential uses; the former for machine tools requiring high hardness and stiffness, and the latter for drill bits requiring high hardness and toughness. Layered superhard-faced cBN composites, designed to satisfy impedance mismatch requirements, also have potential applications in lightweight personnel and vehicular armor.

$$\underline{3BN} + 3Ti \rightarrow TiB_2 + 2TiN + \underline{BN}\ \text{(un-reacted)} \qquad (2)$$

$$2BN + \underline{4Ti} \rightarrow TiB_2 + 2TiN + \underline{Ti}\ \text{(un-reacted)} \qquad (3)$$

Similar effects are expected for reactive-HPHT processing of BN with Ti, Zr, Hf or mixtures thereof, which opens opportunities for the synthesis of ultra-high temperature ceramics for the next generation of hypersonic vehicles. Currently, the most promising materials are HfB_2, HfC, HfN and their composites, because of their exceptionally high melting points and good oxidation resistance; the latter due to the formation upon oxidation

of a thermally-stable protective scale of HfO_2. Such is not the case for Ti-base compounds, where oxide scales are not stable at high temperatures.

In principle, other compound ceramics (e.g. B_4C and Si_3N_4) and elemental-powder mixtures (e.g. B and C) may also react with Ti, Zr or Hf to form nanostructured composites. For example, reactive-HPHT processing of an appropriate stoichiometric mixture of B_4C+BN+Ti powders should yield a triphasic nanocomposite comprising three distinct phases - TiB_2+TiC+TiN in which one or more phases are extended solid solutions. An important feature of the process is that it can be adapted to make use of today's hot pressing and hot-isostatic pressing technologies, thus there is the prospect of scaling the technology at relatively low cost. Moreover, tailoring the mechanical properties of such a multi-phasic nanocomposite to satisfy the performance requirements of a specific application seems technically feasible. This may provide sufficient incentive to industry to commercialize this new class of nanocomposite ceramics for high-temperature structural applications.

Several publications give detailed descriptions of SHS-based methods to produce refractory materials, including carbides, borides, nitrides, silicides and intermetallics [71-73]. Particularly relevant to the present discussion is research on *dynamic compaction* to produce TiB_2/TiC composites[74-76]. The experimental setup enables reactive consolidation of a well-mixed B_4C and Ti powder in two sequential steps. First, the reactants are ignited by an electrical discharge at the top of a green compact, thereby generating a combustion wave that propagates downward through the entire compact. Second, upon reaching the sample base, an explosive is detonated such that a shock wave propagates through the adiabatically-heated compact. The effect is to achieve rapid powder densification, probably assisted by some melting of the reacting phases. The final fully-

dense composite consists of a uniform distribution of TiB_2 and TiN phases, with average grain size about 3.5 µm.

The present method differs from this earlier work in that much greater flexibility is afforded in control of the scale of the final grain size, ranging from submicron- to nano-scale dimensions, while also retaining some un-reacted Ti to enhance toughness. This is an important consideration, since most of the projected applications for this new class of hard and superhard composites require some degree of toughness. Historically, this was also a requirement in the development of WC/Co hardmetals, where, without the presence of a ductile-Co binder phase for the hard/brittle WC phase, applications would be severely limited. Hence, in future work, we will place much greater emphasis on trade-offs between hardness and toughness by varying the volume fraction ratio of superhard cBN phase and ductile Ti, as has been done for WC/Co hardmetals for decades. In fact, each application today specifies volume fraction ratio of WC/Co phases to obtain just the right combination of hardness, compressive strength, and fracture toughness. Interestingly, in the most recent development in the field, a bimodal-structured WC/Co is gaining prominence, where coarse-grained WC particles are bonded together with a WC/Co nanocomposite. The effect is to dramatically enhance abrasive-wear resistance, since undercutting of the coarse WC particles is prevented.

Looking ahead, therefore, it seems likely that further development of cBN/Ti-base composites will follow a similar path in properties optimization for machine tools and rock-drill bits, where abrasive wear is a serious performance limiting factor. On the other hand, for lightweight armor applications, it seems likely that lower density cBN/Al-base compositions will be preferred. In this case, there is interest in developing a superhard-

faced composite, comprising an outer layer of superhard cBN and a backing layer of tough Ti-bonded TiB_2/TiN nanocomposite, with a compositionally graded interface to enhance bond strength between the dissimilar materials. Development of this new class of lightweight superhard/tough layered composites has now become an important part of an expanded research effort.

H. Future Work

Recognizing the present accomplishments, the following research areas should be considered for future work:

- High-pressure synthesis cBN powder using Mg as a catalyst has been demonstrated, as well as its HPHT consolidation into monolithic nanocrystalline cBN. It remains to eliminate residual hBN in the consolidated product, since its presence adversely affects hardness, strength, and particularly toughness. To do so, the use of sintering aids will be investigated. In addition, a new in-house source of high purity cBN nanopowder, synthesized by plasma decomposition of a borane-ammonia precursor, will be used in future consolidation work. At the same time, we will collaborate with Diamond Innovations to investigate scaling of the processing technology, with the objective of being able to fabricate, for the first time, large panels of superhard nanocrystalline cBN for lightweight personnel and vehicular armor.
- High-pressure consolidation of a new class of cBN/Ti-base composites, comprising a high fraction of superhard cBN particles in a tough Ti matrix or binder phase, has been demonstrated. Most importantly, it has been shown that the pressure requirements to achieve complete consolidation is as low as 0.1 GPa, so that scaling using HIP technology becomes technically feasible. To explore this option, we will collaborate with Diamond Innovations.
- High-pressure consolidation of a multi-layered structure has been demonstrated, but much remains to be done to suppress undesirable reactions with the graphitic-carbon heater, and to control interphase-interface properties to avoid delamination between layers due to thermal-expansion and elastic-modulus misfit stresses.

- From a more fundamental perspective, it is of interest to obtain a better understanding of mechanisms and kinetics involved in HPHT powder consolidation, when it is accompanied by a strong exothermic reaction. A preliminary assessment indicates that an uncontrollable run-away reaction can be avoided by adjusting the mixing scale of the reacting powders.

Appendix A

Considerable effort has been devoted to polishing nanocrystalline cBN samples in order to make reliable hardness measurements. However, even using the best grinding and polishing practice, the surface finish is poor. ***Figure A.1*** shows an example of a pitted surface on a sample of powder #1 after consolidation at 8.0 GPa/1000ºC/15 min. The pitting effect is ascribed to grain pull-out during polishing with a fine-diamond paste. Also shown is a Vickers hardness indent (arrow) that is located in a pitted area of the sample. Not surprisingly, the measured hardness at this location is lower (40-50 GPa) than that of nano-grained material (85 GPa). Even so, scratch tests indicate an exceptionally hard material.

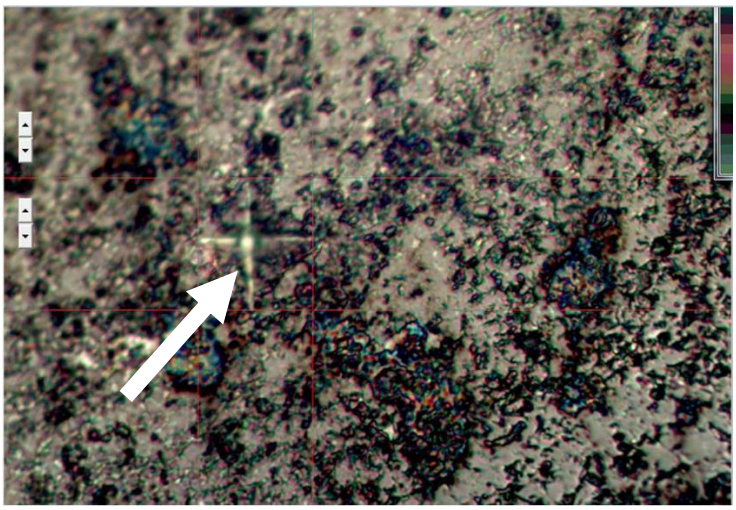

Figure A.1 - Example of the pitted surface of a consolidated sample of powder#1, showing extensive grain pullout due to polishing. Also shown is a Vickers hardness indent (arrow).

Surface pitting is such a reproducible effect in diamond-polished samples that it must reflect an intrinsic characteristic of the HPHT-consolidated cBN. One possible explanation

is that the superhard material contains internal micro-strains that are not relaxed at the 1000ºC processing temperature. Hence, a post-annealing treatment, say at a temperature >1600ºC may be necessary to induce recovery and/or recrystallization, thereby achieving a strain-free nanocrystalline product.

To test this hypothesis, a comparison will be made of polished surfaces on as-consolidated and post-annealed samples. In addition, the synchrotron method, developed by Tsakalakos et al. [43], will be used to measure the internal-strain distribution, and changes with increasing depth in the consolidated disc-shaped sample. Information on sample texturing may also be obtained, which is of interest since evidence for texturing is observed by TEM, ***Figure 25*****.** It is an interesting question whether micro-strained cBN offers an advantage in terms of ballistic-impact performance, since it may promote powderization at the impact location, accompanied by significant energy absorption.

Since there are many small areas of the pitted sample that are quite smooth in appearance, ***Figure A.1*****,** nanoindentation testing provides a means to measure hardness in such areas. Results obtained for this particular sample are presented in ***Figure A.2***. As expected, the nanoindenter is able to obtain data for smooth areas of the sample. The upper hardness value is ~75 GPa, in line with a reported value of 85 GPa [11]. As an additional point of comparison, the hardness of nanocrystalline cBN is well over 9 on Mohs scale.

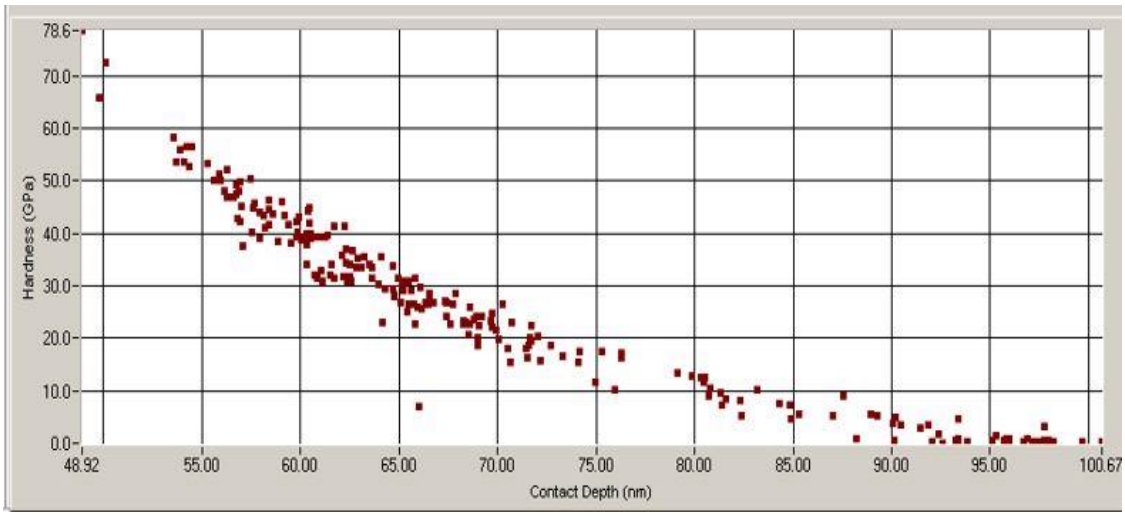

Figure A.2 - Nanoindentation data for a nano-cBN sample, after HPHT consolidation of powder #1 at 8.0 GPa/1000ºC/15min

A similar problem is encountered in polishing consolidated samples of powder #2, processed under essentially the same conditions as powder #1. However, in this case, the polishing problem is exacerbated by the presence of residual micro-porosity in the HPHT-processed cBN. Thus, a sample processed at 8.0 GPa/1600ºC/10 min, with 93.7 % theoretical density, gives a relatively low hardness value of 20 GPa, which is ascribed to the presence of residual micro-porosity. Even so, the hardness of the consolidated cBN is well above 9 on Mohs scale.

With regard to cBN/Ti compositions, once again difficulties are encountered in obtaining smooth surfaces on consolidated samples, irrespective of whether the starting material is powder #1 or powder #2. Best results are obtained for 50:50 cBN:Ti mixtures, using powder #2, consolidated at 0.3 GPa/1000ºC/15 min. Vickers hardness values at loads well into the macro-hardness range give values of 35 GPa, whereas reported values for TiN (18-24 GPa) and TiB_2 (25-35 GPa). The higher hardness of the HPHT-processed

material is attributed to its nanocomposite structure. Unfortunately, due to polishing limitations, it is not possible to evaluate fracture toughness. To overcome this shortcoming, additional work is being performed to improve polishing procedure so as to observe corner cracking at indents, as required to determine toughness.

To summarize, presently there is some uncertainty in the hardness values of HPHT-processed samples due to pitting of their polished surface. Surface pitting is attributed to two main causes: high levels of internal micro-strains and/or micro-porosity. Modified HPHT processing parameters, along with improved polishing and evaluation techniques, will be investigated in future work. Both are important to the continued development of nanostructured hard and superhard cBN-base materials for lightweight armor applications.

References

[1] J. Wentorf and E. Al., “Diamond tools for machining - US Patent 3745623.” 1973.

[2] R. H. Wentorf, R. C. Devries, and F. P. Bundy, “Sintered superhard materials.,” *Science*, vol. 208, no. 4446, pp. 873–80, May 1980.

[3] R. H. Wentorf, “Synthesis of the Cubic Form of Boron Nitride,” *J. Chem. Phys.*, vol. 34, no. 3, p. 809, 1961.

[4] F. P. Bundy and R. H. Wentorf, “Direct Transformation of Hexagonal Boron Nitride to Denser Forms,” *J. Chem. Phys.*, vol. 38, no. 5, p. 1144, 1963.

[5] J. Angseryd, M. Elfwing, E. Olsson, and H.-O. Andrén, “Detailed microstructure of a cBN based cutting tool material,” *Int. J. Refract. Met. Hard Mater.*, vol. 27, no. 2, pp. 249–255, Mar. 2009.

[6] C. S. Pande and K. P. Cooper, “Nanomechanics of Hall–Petch relationship in nanocrystalline materials,” *Prog. Mater. Sci.*, vol. 54, no. 6, pp. 689–706, Aug. 2009.

[7] H. Kuwahara, N. Mazaki, M. Takahashi, T. Watanabe, X. Yang, and T. Aizawa, “Mechanical properties of bulk sintered titanium nitride ceramics,” *Mater. Sci. Eng. A*, vol. 319–321, pp. 687–691, Dec. 2001.

[8] K. M. Taylor and C. Lenie, “Some Properties of Aluminum Nitride,” *J. Electrochem. Soc.*, vol. 107, no. 4, p. 308, 1960.

[9] Y. Tian, B. Xu, D. Yu, Y. Ma, Y. Wang, Y. Jiang, W. Hu, C. Tang, and Y. Gao, “Ultrahard nanotwinned cubic boron nitride,” *Nature*, vol. 493, pp. 385–388, 2013.

[10] ASM International, *Engineered Materials Handbook Volume 4, Ceramics and Glasses*. ASM International, 1991, p. 819.

[11] N. Dubrovinskaia, V. L. Solozhenko, N. Miyajima, V. Dmitriev, O. O. Kurakevych, and L. Dubrovinsky, “Superhard nanocomposite of dense polymorphs of boron nitride: Noncarbon material has reached diamond hardness,” *Appl. Phys. Lett.*, vol. 90, no. 10, p. 101912, 2007.

[12] V. L. Solozhenko, O. O. Kurakevych, and Y. Le Godec, “Creation of nanostuctures by extreme conditions: high-pressure synthesis of ultrahard nanocrystalline cubic boron nitride.,” *Adv. Mater.*, vol. 24, no. 12, pp. 1540–4, Mar. 2012.

[13] H. Lee and R. F. Speyer, “Hardness and Toughness of Pressureless Sintered Boron Carbide (B4C),” *J. Am. Ceram. Soc.*, vol. 93, pp. 1291–1293, 2002.

[14] R. G. Munro, “Material properties of titanium diboride,” *J. Res. Natl. Ist. Stand.*, vol. 105, no. 5, pp. 709–720, 2000.

[15] J. Tse, D. Klug, and F. Gao, “Hardness of nanocrystalline diamonds,” *Phys. Rev. B*, vol. 73, no. 14, p. 140102, Apr. 2006.

[16] V. L. Solozhenko and O. O. Kurakevych, “Chemical interaction in the B–BN system at high pressures and temperatures.,” *J. Solid State Chem.*, vol. 182, no. 6, pp. 1359–1364, Jun. 2009.

[17] CAlphad Thermodynamic Database, “Titanium-Boron Phase Diagram.” p. 3500, 2008.

[18] K. Leinenweber, J. Tyburczy, T. Sharp, E. Soignard, D. Tamara, W. Petuskey, Y. Wang, and J. Mosenfelder, “Cell assemblies for reproducible multi-anvil experiments (the COMPRES assemblies),” *Am. Mineral.*, vol. 97, pp. 353–368, 2012.

[19] N. Shin-ichi, Hirano, Naka Shigeharu, “Methods for Preparing Cubic Boron Nitride Sintered Body US Patent 4,545,968,” 1985.

[20] O. O. Kurakevych and V. L. Solozhenko, “Experimental study and critical review of structural, thermodynamic and mechanical properties of superhard refractory boron suboxide B6O,” *J. Superhard Mater.*, vol. 33, no. 6, pp. 421–428, Dec. 2011.

[21] Y. Tian, B. Xu, and Z. Zhao, “Microscopic theory of hardness and design of novel superhard crystals,” *Int. J. Refract. Met. Hard Mater.*, vol. 33, pp. 93–106, Jul. 2012.

[22] R.-Q. Zhang, T.-H. Lee, B.-D. Yu, C. Stampfl, and A. Soon, “The role of titanium nitride supports for single-atom platinum-based catalysts in fuel cell technologyw,” *Phys. Chem. Chem. Phys.*, vol. 14, no. 48, pp. 16552–7, Dec. 2012.

[23] V. L. Solozhenko and V. Z. Turkevich, “Refined Phase Diagram of Boron Nitride,” *Am. Chem. Soc.*, vol. 103, pp. 2903–2905, 1999.

[24] C. S. DANA, James Dwight, Hurlbut, *Dana’s Manual of Minerology (17th Edition)*, 17th Editi. New York, Chapman HAll, 1959, pp. 78–89.

[25] V. L. Solozhenko, D. Häusermann, M. Mezouar, and M. Kunz, “Equation of state of wurtzitic boron nitride to 66 GPa Equation of state of wurtzitic boron nitride to 66 GPa,” *Appl. Phys. Lett.*, vol. 72, number, no. 1691, pp. 1691–1693, 1998.

[26] Z. Pan, H. Sun, Y. Zhang, and C. Chen, “Harder than Diamond: Superior Indentation Strength of Wurtzite BN and Lonsdaleite,” *Phys. Rev. Lett.*, vol. 102, no. 5, p. 055503, Feb. 2009.

[27] J. E. Laurence Vel, Gerard Demazeau, “Cubic boron nitride: synthesis, physiochemical properties and applications,” *Mater. Sci. Eng. B*, vol. 10, no. 2, pp. 149–164, 1991.

[28] J. Schmidt, M. Boehling, U. Burkhardt, and Y. Grin, “Preparation of titanium diboride TiB 2 by spark plasma sintering at slow heating rate,” *Sci. Technol. Adv. Mater.*, vol. 8, no. 5, pp. 376–382, Jul. 2007.

[29] R. Riedel, *Handbook of Ceramic Hard Materials*, Volume 1. Wiley-VCH, 2004, p. 185.

[30] J. L. Wreidt, H.A. Murray, “The N-Ti (Nitrogen-Titanium) System,” *Bull. Alloy Phase Diagrams*, vol. 8, no. 4, pp. 378–379, 1987.

[31] K. Yamada, Shimada, “Properties of Bulk Titanium Nitiride,” *Am. Ceram. Soc. Bull.*, vol. 59, p. 611, 1980.

[32] H. Okamoto, “Phase Diagram of Titanium Nitride,” *J. Phase Equilibria Diffus.*, vol. 34, no. 2, pp. 151–152, Oct. 2012.

[33] S. Deutsch, “High Pressure Phase Transformations in Polycrystalline Yttrium Oxide,” Rutgers University, Dept of Matl. Science & Engineering, 2012.

[34] O. A. Voronov and B. H. Kear, “Method for Rapidly Synthesizing Monolithic Polycrystalline Diamond Articles US PAtent 8,021,639 B1,” 2011.

[35] O. A. Voronov and L. S. Kashevarova, “Low-Temperature Synthesis of Cubic Boron Nitride and Diamond Under high Pressure,” in *electrochemical Society Proceddings Volume 95-4*, 1995, pp. 318–323.

[36] O. A. Voronov, G. S. Tompa, and B. H. Kear, “High Pressure-High Temperature Device for making Diamond Materials,” *Electrochem. Soc.*, vol. 25, pp. 264–271, 2001.

[37] N. Velisavljevic, S. Macleod, and H. Cynn, “Titanium Alloys at Extreme Pressure Conditions,” *Surf. Coatings Technol.*, vol. 125, pp. 335–340, 2000.

[38] O. Voronov, “Pressure Dependency of Tm (oC) of Mg, Al, Ti Pressure (GPa),” p. 2500, 2000.

[39] J. D. Cullity, *Elements of X-Ray Diffraction*, Second. Addison-Wiley, 1978, p. 102.

[40] MDI Coporation, “Jade Software Ver 9.6.0 4-11-14.” 2014.

[41] F. Karlsruhe, “Inorganic Crystal Structure Database (ICSD).” 2014.

[42] R. L. Jenkins, R Snyder, *Introduction to X-ray Powder Diffractometry*. John Wiley and Sons, Inc., 1996, pp. 89–91.

[43] T. Tsakalakos and M. Croft, "XRD Strain and Stress Determination in Nanostructured Films and Coatings," in *NATO Advanced Research Workshop on Nanostructured Films and Coating*, 2000, pp. 223–230.

[44] B. E. Warren, *X-Ray Diffraction*. Addsion-Wesley Publishing Co., 1969, pp. 251–254.

[45] H. P. Klug and L. E. Alexander, *X-Ray Diffraction Procedures*. John Wiley & Sons Inc., 1974, pp. 687–703.

[46] J. Ghosh, S. Mazumdar, M. Das, S. Ghatak, and a. K. Basu, "Microstructural characterization of amorphous and nanocrystalline boron nitride prepared by high-energy ball milling," *Mater. Res. Bull.*, vol. 43, no. 4, pp. 1023–1031, Apr. 2008.

[47] R. A. Young, "Crystal Imperfection Broadening and peak shape in the Reitveld Method," in *The Reitveld Method*, Oxford University Press 1995, 1995, pp. 133–163.

[48] J. J. Friel, *X-Ray and Image Analysis in Electron Microscopy*, 2nd ed. Princeton Gamma Tech, 2003, p. 97.

[49] Zeiss, *Zeiss Field Emission Scanning Electron Microscope Users Guide*. 2005, p. all.

[50] D. Williams and B. Carter, *Transmission electron Microscopy*. Plenum Press, 1996.

[51] T. L. Heath, *The Works of Archimedes*, 1st ed. London: Cambridge University Press, 1897, p. 65.

[52] ASTM International, "ASTM E384 Standard Test Method for Knoop and Vickers Hardness of Materials." ASTM International, West Conshohocken, PA, pp. 1–43, 2014.

[53] ASTM International, "ASTM C1327 Standard Test Method for Vickers Indentation Hardness of Advanced Ceramics." ASTM International, West Conshohocken, PA, pp. 1–9, 2014.

[54] J. Morgiel and E. Benko, "Microstructure of boron nitride sintered with titanium," *Mater. Lett.*, vol. 25, no. October, pp. 49–52, 1995.

[55] M. T. B. Wreidt, Murray, "Phase Diagram of Binary titanium Alloys," in *ASM Inetrnational*, 1990, p. 176.

[56] I. Song, L. Wang, and M. Wixom, “Self Propogating High Temperature Synthesis and Dynamic Compaction of titanium diboride/titanium carbide Composites,” *J. Mater. Sci.*, vol. 35, pp. 2611–2617, 2000.

[57] E. K. Storms, *The Refractory Carbides*. New York: Academic Press, 1967.

[58] L. E. Toth, *Transition Metal Carbides and Nitrides*. New York: Academic Press, 1971.

[59] J. A. Puszynski, *Carbide, Nitride, and Boride Materials*. London: Chapman & Hall, 1997, pp. 183–228.

[60] Z. A. Munir and U. Anselmi-Tamburini, “Self-propogating exothermic reactions: the synthesis of high temperature materials by combustion,” *Mater. Sci. Reports*, vol. 3, no. 7, pp. 277–365, 1989.

[61] J. J. Moore and H. J. Feng, “Combustion Synthesis of Advanced Materials,” *Prog. Mater. Sci.*, vol. 39, pp. 277–365, 1995.

[62] R. Pampuch, “Advanced HT Ceramic Materials via Solid Combustion,” *J. Eur. Ceram. Soc.*, vol. 19, pp. 2395–2404, 1999.

[63] J. B. Holt and Z. A. Munir, “Combustion Synthesis of Titanium Carbide, theory and experiment,” *J. Mater. Sci.*, vol. 21, pp. 251–259, 1996.

[64] F. Bernard and E. Gaffet, “Mechanical Alloying in SHS Research,” *Int. J. SHS*, vol. 10, no. 2, pp. 109–132, 2001.

[65] S. . Roy, A. Biswas, and S. Banerjee, “Self-propogating high-Temperature Synthesis of Titanium Borides,” *Bull. Mater. Sci.*, vol. 16, no. 5, pp. 347–356, 1993.

[66] R. Pampuch, “Some Fundamental Versus Practical Aspects of Self Propogating High-temperature Synthesis,” *Solid State Ionics*, vol. 101, pp. 899–907, 1997.

[67] S. K. Roy and A. Biswas, “Combustion Synthesis of TiB and TiB2 Under Vacuum,” *J. Mater. Sci. Lett.*, vol. 13, p. 371, 1994.

[68] US National Research Council, *Strategic Technologies for the Army of the Twenty-First Century*. Washington, D.C: National Academy Press, 1992, pp. 159–169.

[69] J. J. Moore and H. J. Feng, *Progress in Material Science, Combustion Synthesis of Advanced Materials*. Tarrytown New York: Elsevier Science Ltd., 1995, pp. 241–73.

[70] R. Mackenzie, *Differential Thermal Analysis*, 2nd ed. London: Academic Press, 1970, pp. 38–59.

[71] S. D. Dunmead, *Carbide, Nitride, and Boride Materials Synthesis and Processing*. London: Chapman & Hall, 1997, pp. 229–272.

[72] A. G. Merzhanov and S. Y. Shraivker, *Self Propogating high temperature synthesis of carbides, nitrides, and borides*. Netherlands: Kluwer Academic Publishers, 1999, pp. 205–202.

[73] T. Kim and M. S. Wooldridge, "Catalytically Assisted Self-propagating High-temperature Synthesis of tantalum carbide Powders," *J. Am. Ceram. Soc.*, vol. 84, no. 5, p. 2001, 2001.

[74] L. Wang, M. Wixom, and L. T. Thompson, "Structural and Mechanical Properties of TiB2 and TiC Prepared by self-Propogating high-temperature Synthesis/dynamic Compaction," *J. Mater. Sci.*, vol. 29, no. 2, pp. 534–543, 1994.

[75] S. K. Mishra, S. K. Das, and V. Shcherbakov, "Effect of Alumina Diluent on the Fabrication of In-Situ Al 2 O 3 -Ti / ZrB 2 Composite by Self Propagating High Temperature Synthesis Dynamic Compaction," *Metall. Mater. Trans. B*, vol. 37B, pp. 2006–2641, 2005.

[76] P. Boogard, "Dynamic Compaction of Ceramics," Delfy University, 1995.